Modelling and Analysis of Wirelessly Interrogated SAW based Micropumps for Drug Delivery Applications

by

Don Wenura Eranda Dissanayake

B. Eng Computer Systems (First Class Honours),
University of Adelaide, 2004

Thesis submitted for the degree of

Doctor of Philosophy

in

School of Electrical and Electronic Engineering,
Faculty of Engineering, Computer and Mathematical Sciences
The University of Adelaide

April 2010

Chapter 1

Introduction and Motivation

THIS Chapter introduces demanding requirements for design, development, and analysis of novel Micro Electro Mechanical Systems (MEMS) based implantable drug delivery devices. The suitability of modelling and simulation methodologies are discussed in relation to numerical modelling and analysis of microstructures and microfluidic devices.

Additionally, this chapter outline the motivation for this research, and objectives of this thesis. The thesis overview is also provided and the content of each Chapter are outlined. Finally, the original and novel contributions of this thesis are summarised.

1.1 Biomedical Implants and Healthcare

Future biomedical implants with extended and easy to use wireless connectivity and secure interrogation will form a critically important platform of an intelligent health care delivery systems and infrastructure. Currently, common areas of application of implants include, total drug delivery systems for diagnostic and treatment of various disorders such as pain relief and diabetes, orthopedic implants such as bone screws and plates, reconstructive prosthesis implants, and cardiac prostheses implants such as heart valves, and cornea implants.

Remotely interrogated implants such as, remotely powered implantable microsystem for blood glucose monitoring (Ahmadi and Jullien 2009), remote sensor system for the detection of heartbeat and respiration rate (Choi and Kim 2009), are some of the recent advancements.

Additionally, there are a number of other implants in use, in relation to restoring a range of critical human functionalities such as brain pacemakers for treatment of Parkinson's disease, cochlea implants, artificial eyes (Cavuoto 2004), muscle stimulators, and nerve signal recorders for use with robotic prostheses (Weir *et al.* 2003, Johansson 2004). Moreover, the implants for drug delivery have become so critical, and the development of various technologies for attractive micro drug delivery devices is of high interest (Tsai and Sue 2007, Ranade and Hollinger 2004).

1.1.1 Implants for Drug Delivery

The number of patients suffering from life threatening global health problems and chronic diseases such as cardiovascular deceases (hypertension, heart attack, stroke), septicaemia, cancer, diabetes, melancholia, and malignant lymphoma have increased more than ever before (Ranade and Hollinger 2004). Medical and biological experts view is that early recognition and treatment are the key to eliminate and/or control such risky disorders (Nisar *et al.* 2008d, Lifespan 2009).

Most of the currently existing biomedical implants extract energy from a battery, which is attached to the implant. Even though batteries provide all of the energy needs for implants, batteries inherently limit operating lifetime due to their fixed energy density and the strict volume and mass constraints imposed by implantable devices. Therefore, a new alternative transcutaneous energy transmission system is also highly regarded for microdevices that are targeted at *in–vivo* applications.

On the other hand, conventional drug delivery methods such as oral tablets or injections have various limitations. Among them, the problem of variable absorption profiles and the need for frequent dosing are yet to be addressed (Ranade and Hollinger 2004). Furthermore, conventional controlled–release formulations are designed to deliver drugs at a predetermined, preferably constant rate. Some clinical situations, however, necessitate either an external control of the drug delivery rate, or a volume of drug that is beyond the capabilities of existing controlled-release formulations (Ranade and Hollinger 2004). Therefore, conventional methods are not effective in delivering a drug within their therapeutic range (Tsai and Sue 2007, Razzacki *et al.* 2004).

Therefore, it is evident that novel techniques are required for accurate and effective early diagnostics and/or targeted treatments. Such techniques should incorporate automatic dosing capabilities, so that the patients are prevented from sudden death or irregular/incorrect intake of medicine/drug. Therefore, the implementation of targeted micro drug delivery methods is recognised as one of the critical solutions in the life–saving health advances.

1.1.2 MEMS Technology and Micro Drug Delivery Implants

Due to the rapid growth in Micro Electro Mechanical Systems (MEMS) technology, design, development, and realisation of miniature devices for biomedical implants have become a reality. In particular, Bio–MEMS based implantable micro drug delivery systems have shown the potential to offer new paradigms in biomedicine and biology. Bio–MEMS based micro drug delivery systems consist of various types of MEMS devices such as micropumps, microsensors, microvalves, microneedles, microfluidic channels, and drug reservoirs.

A typical micropump is a fundamental and a critical part of a drug delivery system which provides an actuation source to effectively transfer an accurate amount of fluid/drug to a targeted location. Among the large number of microfluidic components realised up to now, micropumps have clearly represented a critical role in science.

However, the lack of availability of accurate and easy to use, implantable and low-powered micropumps has been identified as a significant problem (Jones *et al.* 2008). Furthermore, the ease of control of implantable biological devices would be greatly

improved by incorporation of wireless and secure actuator systems with no battery attached to the device.

1.1.3 Wireless and Secure Interrogation

With the advancements in RF–MEMS and Bio–MEMS technologies, there is an increasing interest to design biotelemetry devices. Biotelemetry implies the contactless measurement of different electrical and nonelectrical parameters measured from human or animal subjects (Pitz *et al.* 2002). Currently, there are various implants in use and in development (Medtronic Incorporation 2009, Prescott *et al.* 2006).

Especially, remotely interrogated implantable drug pumps have been developed for pain relief applications such as for chronic pain due to cancer, chronic back leg pain, painful neuropathy (Medtronic Incorporation 2009), and Complex Regional Pain Syndrome (CRPS). However, large size due to the in built active electronics has been a major drawback in these devices.

In developing biomedical implants for biological applications, such as micro drug delivery, the importance of wirelessly controlled, implantable microvalves and micropumps is increasing gradually. The most anticipated benefit with wireless control (RF telemetry) is the greater mobility for patients. Furthermore, a wirelessly powered implant with no battery at the implant would add much more benefits to patients. As such, small size, mass, long lifetime of the implant, and the possibility of implanting the device into a wide range of locations within the body are of high impact (Pitz *et al.* 2002, Johansson 2004).

1.2 Modelling and Simulation of MEMS

The development and realisation of new, complex MEMS devices are intensely supported by modern modelling and simulation platforms that are based on Computer Aided Design (CAD) and Computer Aided Modelling (CAM) with numerical simulation tools. Such tools substitute the traditional approaches that were based on experimental investigations with several design and fabrication cycles until the optimal specifications are satisfied.

New CAD and CAM based numerical simulation tools have become an essential key for designing and manufacturing MEMS devices with higher performance and reliability, reduced costs, shorter development cycles and time–saving approaches, compared to the traditional approach. Event though MEMS technology has been known for more than two decades, the commercialisation of MEMS technology has not progressed as fast as Integrated Circuit (IC) technology.

A major technical barrier in the development of novel MEMS devices that have potential applications in biomedical, environmental, military and industrial applications, lies in the lack of understanding of physical phenomena. Moreover, the functionality of most of the advanced MEMS devices made of interactions between few physics fields. Most microdevices rely on interactions of thermal, mechanical, electric, magnetic and/or fluidic fields for performing their intended functions. Therefore, further understanding in multi–physical microsystems is highly regarded in developing advanced MEMS devices.

Similarly, to support the successful implementation of MEMS based drug delivery systems, a spectrum of simulation tools is needed, such that the coupled effects of different physics fields could be analysed simultaneously. In recent times, an increasing trend is identified in the use of Finite Element Modelling (FEM) and Analysis (FEA) tools for RF–MEMS and Bio–MEMS design and simulations. Similarly, FEA based Computational Fluid Dynamics (CFD) is becoming a prominent numerical method in microfluidic flow analysis problems.

1.2.1 Finite Element Modelling (FEM) and Analysis (FEA)

In general, the development of analytical models with better representation of complex models consisting of interactions between multiple–physics fields, requires extensive modelling and computational efforts. It is known that more accurate results for such problems can be achieved through numerical analysis using mathematical methods such as FEM and FEA (Bao 2000, Nisar *et al.* 2008b). Furthermore, existing FEA tools are versatile in modelling complex irregular geometries, allowing detailed visualisation of designed model. FEA software provides a wide range of simulation options for controlling the complexity of both modeling and analysis of a system. Similarly, the desired level of accuracy required and associated computational time requirements can be managed simultaneously to address most engineering applications. FEA allows

entire designs to be constructed, refined, and optimised before the design is manufactured.

Moreover, a range of benefits has substantially increased its usage at various levels in research and development process. Such advantages include; increased accuracy, enhanced design and better insight into critical design parameters, virtual prototyping, fewer hardware prototypes, a faster and less expensive design cycle, increased productivity, within the context of time–to–manufacture of the device.

1.2.2 Computational Fluid Dynamics (CFD)

CFD uses numerical methods and algorithms in fluid mechanics to solve and analyse problems that involve fluid flows. The purpose of carrying out a CFD analysis is to understand how fluid dynamics affects the operation and performance of a device, from a design and analysis perspective. During CFD analysis, the application of the conservation laws with boundary and initial conditions take place in mathematical discretised form in order to estimate field variables (Huebner *et al.* 2001).

Similar to structural models, it is been realised that developing analytical models for fluid flow analysis is much more complex compared to the available numerical methods. Various researchers have successfully utilised numerical methods to model and analyse microfluidic flow in MEMS devices (Olsson 1998, Wang *et al.* 2008, Singhal *et al.* 2004, Rosa and Pinho 2006, Gamboa *et al.* 2005).

A variety of discretisation methods are available for CFD analysis of micro structures. These include Finite Volume Method (FVM), Finite Element Method (FEM), Finite Difference Method (FDM), and Boundary Element Method (BEM). FEM is found to be much more stable than the FVM approach and subsequently it has become the new direction in which CFD is moving (Löhner 2008). Additionally the stability and robustness of the solution is considered to be better in FEM, though for some cases it might take more memory than other numerical methods (Huebner *et al.* 2001). Furthermore, with the availability of sophisticated FEA and CFD tools with multiple coupling capabilities, more complex Fluid–Structure Interaction (FSI) problems can also be accurately modelled.

Therefore, such numerical methods based models of microdevices for implants can be used to investigate the effects of changing parameters and/or geometry with greater certainty, and at substantially less cost than building a new experimental prototype.

Additionally, the simulation of design performance can be utilised to evaluate the safety of the implant or the effect of introducing drugs into a system without endangering human lives. It may serve to provide expert opinion to surgeons in the event of strategising the device implant through better understanding of its operating mechanism.

1.3 Objectives of the Present Research

The first objective of the this thesis is to present numerical simulations based extensive investigations of low–powered microactuators, microdiaphragms, diffuser microvalves, and three dimensional (3D) micropumps that are targeted for implantable biomedical applications such as drug delivery. The second objective is to implement and investigate a novel, secure interrogation mechanism for biomedical implants. The third objective is to develop FEM, and FEA based CFD simulation platforms for accurate modelling and analysis of MEMS devices.

To achieve these objectives, a range of research questions can be asked to identify several gaps in currently existing approaches and methodologies. Especially, related to MEMS interrogation mechanisms, biocompatibility, and numerical modelling and analysis. These questions are:

- How suitable the existing micropumps technology for implantable drug delivery applications?
- How to make use of the existing technology to develop low cost, reliable micropumps with ease of fabrication?
- Given that the size and the mass of an implant have to be miniaturised as much as possible, is it possible to have an implant with no power source attached? If so,
- Is it possible to remotely supply the required power to operate the implant, through wireless interrogation of the device?
- Is it possible to design low–powered MEMS implants by further reducing the required power levels?

- How to incorporate a secure operation, by providing a great protection against spurious RF signals?
- Is it possible to develop a fully passive device with no active electronics?
- What techniques can be used for modelling and analysis of complex microstructures, at modular levels as well as integrated system level?
- Is it possible to carry out advance 3D FSI analysis for MEMS micropumps, while taking in to account the interactions between multiple physics fields?

Therefore, in this research, several significant contributions have made, in order to address these highlighted issues, and are presented in detail, in Section 1.5. A novel actuation mechanism is investigated and presented in the context of microactuators and micropumps. In particular, a novel interrogation mechanism is implemented to securely control these microstructures, where the technology is based on low-powered Radio Frequency (RF) communication, combined with Surface Acoustic Wave (SAW) device technology and electrostatic actuation. Hence the requirement of a battery and active electronics to go with the device is successfully eliminated.

In this study, a valveless micropump is designed for the simplicity and ease of fabrication; consisting of diffuser elements for flow rectification, and a microdiaphragm to generate the pumping effect. Moreover, a SAW correlator was utilised for the secure interrogation, where the device responds only to a unique RF signal, which has the exact code as implanted in the SAW correlator. Furthermore, the design, development, performance analysis, and device optimisation are carried out utilising sophisticated FEA and CFD tools.

1.4 Thesis Overview

In this thesis, each significant stage of research is compiled into a chapter. Therefore, each chapter that is presented in this research represents a key research component and presents a novel contribution.

In Chapter 2, a comprehensive review of micro drug delivery devices and systems is carried out, and proposal for a novel, wireless and batteryless, and secure interrogation mechanism for biomedical implants is presented. Furthermore, a discussion of

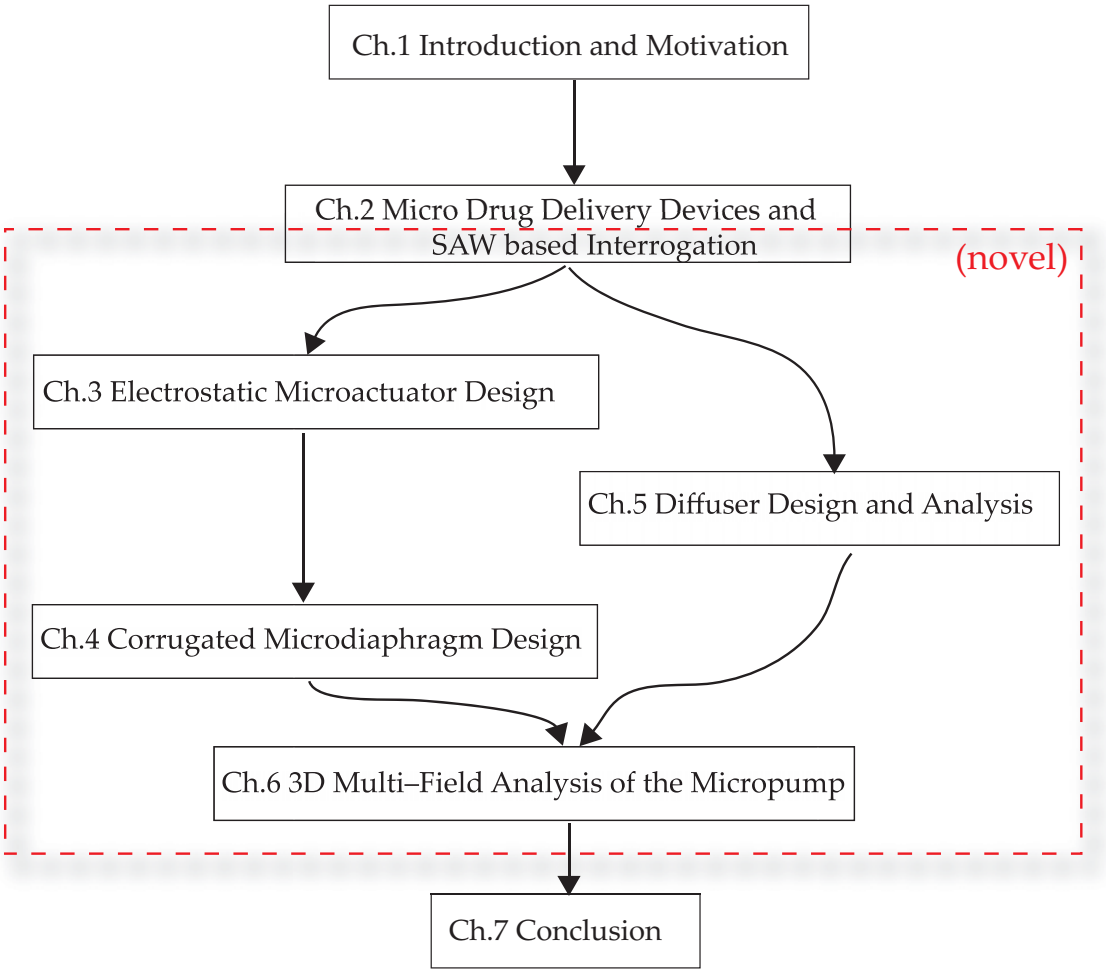

Figure 1.1. Overview of the thesis structure. This flow chart presents the connection between all the Chapters in this thesis. Chapters and segments of Chapters that fall within the dotted red box include original contributions.

SAW device based wireless communication capabilities, in view of their suitability for low–powered implants is presented. This included the proposed novel interrogation mechanism and its secure actuation capability.

Chapter 3 onwards, novel contributions in modelling and analysis of microdevices and components for drug delivery systems are presented. ANSYS and CFX simulation tools are used for FEA and CFD analysis of MEMS devices, respectively. As a result, the use of SAW devices to generate low–powered microactuations is demonstrated. A detailed theoretical analysis is presented, explaining SAW device based actuator operation, and ANSYS based FEA based simulation results are presented and analysed for the SAW actuator model.

Then in Chapter 4, characteristics of a corrugated microdiaphragm for micropumps is presented, and the electrostatic actuation of such a diaphragm using a SAW device is also presented. As an extended analysis from Chapter 3, ANSYS based FEM is performed to evaluate the performance of corrugated microdiaphragms, and the dependency of the performance on different corrugation types, corrugation parameters, material properties, and design practices is also investigated.

Chapter 5 in this thesis concentrate on accurate and effective modelling of micro diffuser/nozzle elements as a flow rectification mechanism for microfluidic devices and systems. Detailed two dimensional (2D) and three dimensional (3D) analysis and results are presented in relation to flat–walled diffusers highlighting their flow rectification capability at low Reynolds numbers.

Chapter 6 presents novel contributions in 3D multi–field modelling and analysis of valveless, SAW based micropumps. Advanced FSI analysis of 3D micropump structures are carried out, utilising FEA based CFD techniques.

Finally, in Chapter 7, a conclusion on the advantages of this study, and a summary of original contributions to the field are made. Furthermore, future vision and novel applications of the associated technology are also carefully recommended.

1.5 Original Contributions

The contributions of this thesis are summarised in this section. The goal of this thesis is to present several significant and novel contributions to the modelling and simulation of MEMS based wireless microactuators and micropumps, microfluidic flow analysis based device optimisation, and advanced computational techniques for Fluid-Solid Interaction (FSI) of coupled–fields. These research contributions are:

- **A Novel Wireless and Secure Interrogation Mechanism:** A novel batteryless and low–powered, secure, and wireless interrogation mechanism for implantable MEMS devices is introduced and investigated. This approach is based on SAW technology and significantly different from currently existing techniques, as the proposed method consists of dual functionality; the interrogation and actuation.
- **A Novel SAW based Wireless and Low–Powered Microactuator:** A new SAW based wireless microactuator is investigated. A theoretical model of the actuation

mechanism is developed, based on the underlying theory on SAW propagation in a piezoelectric media, and electrostatic actuation. Furthermore, the proposed actuator model was implemented and analysed utilising ANSYS based FEA techniques, and results were verified using analytical models.

- **New Combinations and Effective Techniques for Optimisation of Low–Powered Microdiaphragm Performance:** New combinations of attractive methodologies were investigated and developed to optimise the performance of microdiaphragms for low–powered microdisplacements. In view of improving microdisplacements of low profiled microdiaphragms, analysis of the effect of various corrugation profiles on diaphragm performance is presented and FEA based coupled–field analysis techniques were implemented, and various effective approaches were suggested and investigated to enhance the flexibility and stability of low profiled microdiaphragms.

- **A Novel FEA based CFD Analysis of Diffusers under Low Reynolds Number, Laminar Flow Conditions:** Design, analyse and optimisation of diffuser/nozzle based, valveless flow rectification mechanisms for microfluidic devices are presented. As a new contribution, FEA based CFD analysis was utilised to investigate the flow rectification phenomena in 2D and 3D flat–walled diffuser elements, for low Reynolds number and laminar flow conditions. This represents an extension to the currently published research on diffuser flow analysis at design stage, as the analysis that is carried out in thesis provides a qualitative and quantitative relationship between diffuser efficiency and Reynolds numbers.

- **A Novel Methodology for Advanced Analysis of Micropumps with 3D Multi–Field Interactions:** A novel approach is presented in developing advanced modelling and analysis capabilities for low-powered micropumps, especially for an implantable, batteryless, fully passive device that is aimed at micro drug delivery applications. The new 3D modelling and simulation methodology is a combination of 3D multi-field analysis, and multiple code coupling capabilities in commercially available modelling and simulation tools ANSYS and CFX. Both ANSYS based FEA code, and CFX based CFD code were simultaneously combined during the proposed multi–field analysis to simulate the functionality and the flow behaviour of SAW based electrostatically actuated valveless micropump. This Fluid-Solid Interactions (FSIs) between multiple physics fields is effectively

modelled and investigated for both preliminary and fully detailed 3D models of a diffuser/nozzle based micropump.

Chapter 2

Micro Drug Delivery Devices and SAW based Interrogation

THIS chapter introduces MEMS based micropumps and their actuation mechanisms in recognising the significance of such micropumps for *in–vivo* micro drug delivery applications. As a result, a comprehensive review of micropumps, microactuators, and microvalves is presented, in addition to a quantitative and quantitative analysis of such devices.

Additionally, this Chapter introduces a novel interrogation mechanism, as the basis for a wirelessly operated, securely actuated microactuator and micropump designs for biomedical implants such as micro drug delivery. Attractive features and characteristics of Surface Acoustic Wave (SAW) devices, and their utilisation in modern wireless communication is presented, in addition to their usability in the secure interrogation. Moreover, some of the potential biomedical applications of the proposed micropump are also discussed.

2.1 Introduction

MEMS technologies have made it possible to fabricate small size, and high performance implantable devices to meet critical medical and biological needs such as site specific *in–vivo* drug delivery, Lab–on–a–Chip (LoC), micro total analysis systems, and polymerase chain reaction (PCR).

The purpose of this chapter is to provide a comprehensive review of micro drug delivery devices and systems, and propose a novel, wireless and batteryless, and secure interrogation mechanism for biomedical implants. Therefore, an interrogation mechanism, which is based on low–powered RF–MEMS technology, combined with Surface Acoustic Wave (SAW) technology is introduced as the underlying concept for secure actuation of microstructures.

Section 2.2 introduces MEMS based drug delivery systems, and Section 2.3 is focused on reviewing currently existing micropumping and microactuating technologies. Consequently, the flow rectification role of microvalves is reviewed and discussed in Section 2.4, Then, Section 2.5 discusses the functionality of a SAW device, since SAW device performs a major role in the proposed interrogation mechanism, in incorporating batteryless and secure features. Then, the technology behind SAW based wireless communication is also discussed in Section 2.5, in view of highlighting its usefulness in biomedical implants. Then, the proposed novel interrogation mechanism and its secure actuation capability is introduced in Section 2.6. This mechanism is further exploited and thoroughly investigated in Chapters 3 and 4. Moreover, in Section 2.7, some of the potential biomedical applications of the proposed micropump are presented, and proceeded by a conclusion in Section 2.8 .

2.2 MEMS based Drug Delivery Systems

The utilisation of MEMS for biological purposes (Bio–MEMS) has attracted the attention of many researchers around the globe. There is a growing trend to fabricate micro drug delivery systems with newly well developed MEMS fabrication technologies, and are increasingly being applied in medical fields.

A microscale drug delivery system consists of micropumps, microsensors, microvalves, microneedles, microfluidic channels, drug reservoirs and electronic circuits if required (Nisar *et al.* 2008a, Tsai and Sue 2007, Li *et al.* 2004). Such a system is mainly aimed at

abrupt life threats such as heart attack, stroke, septicaemia or serious chronic diseases such as diabetes, melancholia, and malignant lymphoma. With an automatic dosing system being active, sudden death could be prevented, in addition to reducing the risk of irregular/incorrect intake of medicine/drug.

Since microscale drug delivery systems are employed in human bodies, these systems must be safe, and biocompatible (Tsai and Sue 2007). Additionally, the driving voltage level is one of the key constrains that need to be carefully designed for micro–dosing systems. Usually the driving power is expected to be restricted in low electrical energy consumption.

In the event of developing novel microfluidic devices for fluid transfer, one of the primary goals, of course, is to realise an appropriate pumping mechanism. Among the large number of microfluidic components realised up to now, micropumps have clearly represented a critical role in science.

2.3 Micropumps

Micropump is a major component of a MEMS drug delivery system, and it consists of a microactuation mechanism, microvalves, microfluidic chamber (microchannel), and inlet and outlet. The following section provides a detailed review of micropumps commonly used in biomedical applications.

A typical micropump provides an actuation source to dispense drugs or therapeutic agents into a targeted area in the body with precision, accuracy and reliability. Micropumps are therefore an essential component in the drug delivery systems that depend on the targeted application.

Moreover, micropumps are also an essential component in fluid transport systems such a micrototal analysis systems, point of care testing systems and Lab-on-a-Chip (LoP). Micropumps are used as a part of an integrated LoC consisting of microreservoirs, microchannels, micro filters and detectors for precise movement of chemical and biological fluids on a micro scale. Point of care testing system is a micrototal analysis systems to conduct diagnostic testing on site close to patients to provide better health care and quality of life. In such diagnostic systems, MEMS micropumps are integrated with biosensors on a single chip to realise smart devices.

The first micropump based on silicon microfabrication technologies was patented in 1984 and was later published by Smits (1990). That micropump was a peristaltic pump

consisting of three active valves actuated by piezoelectric discs. Importantly, the device was primarily developed for use in controlled insulin delivery systems. Since then, great advancements in micropump technology have been demonstrated for both biomedical and non–biomedical applications.

In general, based on the actuation mechanism, micropumps can be classified as either mechanical or non-mechanical micropumps (Wang and Soper 2007, Nguyen *et al.* 2002). Mechanical type needs a physical actuator or mechanism to perform pumping function. On the other hand, the non–mechanical type of micropumps has to transform certain available non–mechanical energy into kinetic momentum so that the fluid in microchannels can be driven.

A classification of micropumps is presented in Figure 2.1. Various types of commonly used mechanical micropumps are discussed here; including electrostatic, piezoelectric, electromagnetic, thermo–pneumatic, Shape Memory Alloy (SMA), bimetallic, and Ionic Conductive Polymer Film (ICPF). Whereas, non–mechanical micropumps include magnetohydrodynamic (MHD), electrohydrodynamic (EHD), electroosmotic (EO), electrochemical, osmotic–type, electrowetting (EW), Flexural Planar Wave (FPW), and bubble type micropump.

2.3.1 Mechanical Micropumps

Mechanical micropumps also commonly called reciprocating micropumps, use the oscillatory movement of mechanical parts to transfer mechanical energy into fluid movement. In a drug delivery application, the drug from these micropumps is delivered in a series of small discrete volumes, which make up a pulsating flow. Various types of mechanical micropumps that are related to micro drug delivery systems, are reviewed in this section.

Electrostatic

In electrostatic micropump, the membrane (microdiaphragm) of the electrostatic micropump is forced to deflect in either direction as a control voltage is applied on the two opposite electrostatic plates located on both sides as depicted in Figure 2.2. This behaviour is based on the well known Coulomb's law. The deflected membrane is returned to its initial position if the applied voltage is switched off (Judy *et al.* 1991,

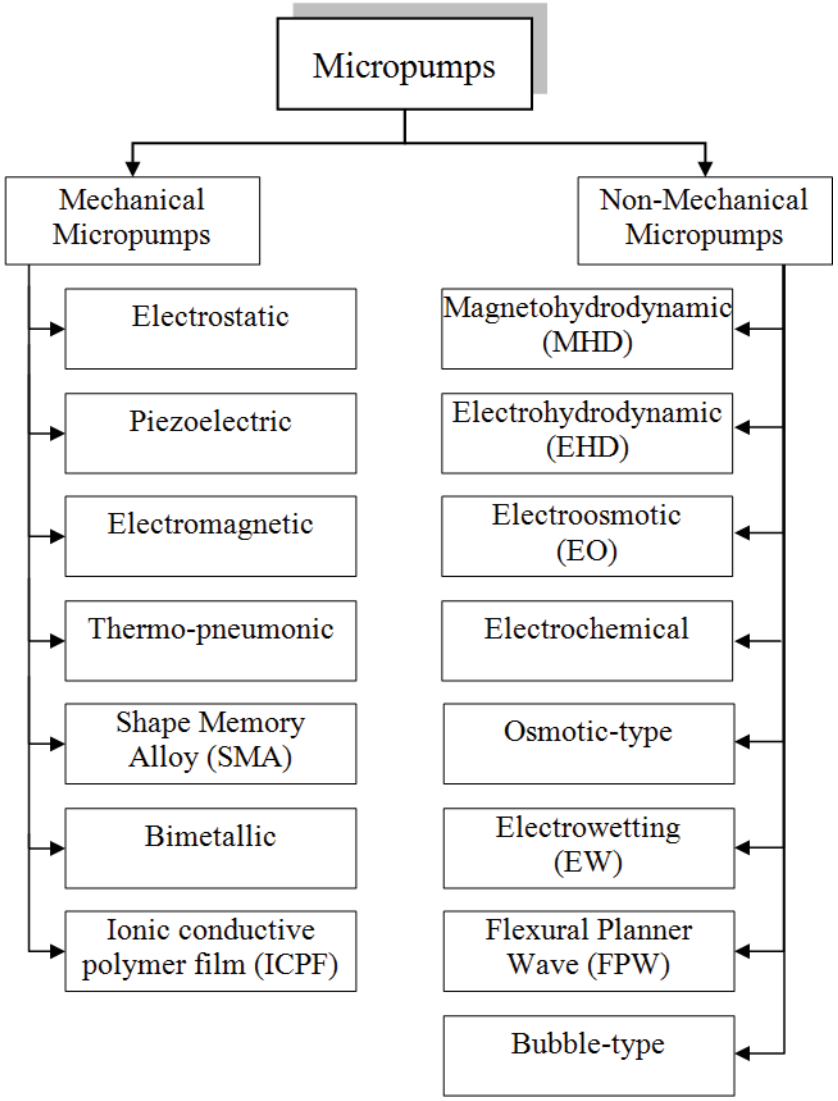

Figure 2.1. Micropump Classification. Different types of mechanical and non–mechanical micropumps.

Zengerle *et al.* 1992, Cabuz *et al.* 2001). Therefore, the chamber volume inside the micropump can be varied by alternating the applied voltage.

A drug reservoir is generally connected to the inlet of the micropump, and the fluid in reservoir is forced to flow in the microchannels due to pressure difference induced by the membrane deflection in the pump chamber.

The main advantages of electrostatic micropumps are fast response time and low power consumption which is generally of the order of 1 mW. Additionally, the deflection of the microdiaphragm can be easily controlled either by modifying the applied voltage, or frequency. A major disadvantage of traditional type electrostatic micropumps is the

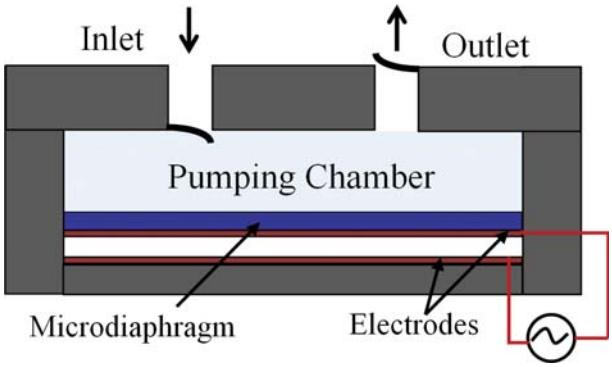

Figure 2.2. Electrostatic micropump. The actuation is based on the Coulomb's law. Two parallel conductive plates are placed in few micrometers apart, and one of them is connected to a flexible microdiaphragm. The control voltage is applied across these electrodes, and hence the electrostatic force is generated between the plates. Then the flexible microdiaphragm is deflected as a function of the applied voltage.

small actuator stroke, which is usually limited up to a few micrometers with an applied actuation voltages in the order of 200 V (Nisar *et al.* 2008a).

As mentioned earlier, the first attempt for developing an electrostatic actuation based micropump with active valves, was presented by Judy *et al.* (1991), however pumping action in this micropump was not reported. Consequently Zengerle *et al.* (1992) developed the first working electrostatically actuated micropump with cantiliver type passive valves. The micropump was made of silicon and had a size of 98 mm^3. Pumping was achieved for the first time at an actuation frequencies in the range of 1 – 100 Hz. For a frequency of 25 Hz and an actuation voltage of 170 V, a flow rate of 70 μl/min at zero back pressure was achieved.

Since then, researchers have designed and developed electrostatic micropumps for various biomedical applications (Teymoori and Abbaspour-Sani 2004), including drug delivery (Bourouina *et al.* 1997). Interestingly, MacHauf *et al.* (2005) contributed to the development of electrostatic pumping mechanisms by fabricating a membrane micropump that was electrostatically actuated across the working fluid. Impressive fact was that such a design has achieved a flow rate of 1 μl/min at 50 V, which is low compared to actuation voltages reported in other designs (Zengerle *et al.* 1992, Zengerle *et al.* 1995, Cabuz *et al.* 2001). However, a major limitation of this design was that the micropump is limited to pump only conductive fluids, and hence restricted its application domain. Overall, electrostatic micropumps have demonstrated flow rates in the range of 1 – 200 μl/min (Zengerle *et al.* 1992, Zengerle *et al.* 1995,

Cabuz *et al.* 2001, MacHauf *et al.* 2005), that are attractive for targeted drug dossing applications (Teymoori and Abbaspour-Sani 2004), and chemical and biological sensing (Cabuz *et al.* 2001).

Piezoelectric

As depicted in the concept design shown in Figure 2.3, a piezoelectric micropump consists of a piezoelectric disk attached on a diaphragm, a pumping chamber and microvalves, where the actuation is caused by the deformation of the piezoelectric materials such as quarts, Lead Zirconate Titanate (PZT), Zinc Oxide (ZnO) (Nguyen *et al.* 2002). Piezoelectric actuation involves the strain induced by an applied electric field on the piezoelectric crystal that behaves like a push plate to expel the fluid out of the chamber.

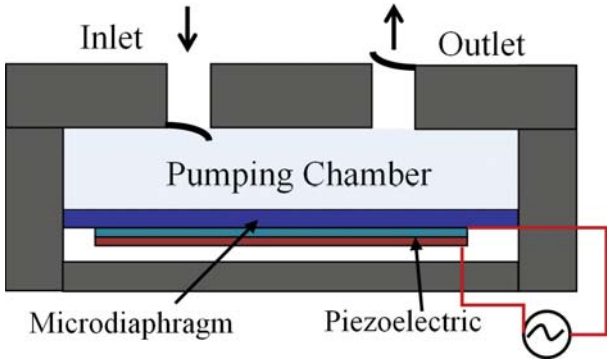

Figure 2.3. Piezoelectric micropump. Piezoelectric micropump consists of a piezoelectric disk attached on a diaphragm, a pumping chamber and microvalves. The actuation is caused by the deformation of the piezoelectric materials.

The advantages and typical characteristics of piezoelectric micropumps include large actuation force, fast response time and simple structure (Nguyen *et al.* 2002). Even though piezoelectric micropumps can be operated at relatively high frequencies, the required induced voltage has to be above a certain level, which is a main limitation for implantable drug delivery applications. despite the simple structure, the fabrication is considered to be complex as piezoelectric materials are not easily processed. The small displacement per unit length (stroke) is also regarded as a disadvantage in piezoelectric micropump, especially for implants. The first attempt to fabricate a silicon micropump based on piezoelectric actuation is reported by Van Lintel *et al.* (1988). This reciprocating displacement type micropump is comprised of a pump chamber,

a thin microdiaphragm which was actuated by piezoelectric disc, and passive silicon check valves to modulate the flow. It was reported that this was the first successfully fabricated micropump using micromachining technologies (Nisar *et al.* 2008a).

Piezoelectric micropumps have been designed and developed for various biomedical applications such as insulin delivery (Koch *et al.* 1998, Ma *et al.* 2006), *in-vivo* drug delivery (Junwu *et al.* 2005, Feng and Kim 2005, Hsu *et al.* 2008), and point of care testing (POCT) (Hsu *et al.* 2008, Suzuki *et al.* 2007).

In most of the piezoelectric micropumps, high flow rates ranging from 100–4000 μl/min have been reported, but in some cases, by trade off the actuating voltages for a higher flow rate (Koch *et al.* 1998).

Therefore, the major limitation of the piezoelectrically actuated micropumps is the requirement for high supply voltages. In addition, the application of piezoelectric discs is not compatible with integrated fabrication. Nevertheless, optimisation of the geometrical design of piezoelectric micropump has been conducted to achieve higher strokes at lower voltages (Linnemann *et al.* 1998, Morris and Forster 2000) to make them more attractive for implantable applications such as low powered drug delivery.

Electromagnetic

As depicted in Figure 2.4, a typical magnetically actuated micropump consists of a chamber with inlet and outlet valves, a flexible diaphragm, a permanent magnet and a set of drive coils. Generally, either the magnet or the set of drive coils may be attached to the diaphragm. As an electric current is driven through the drive coils, the resulting magnetic field creates an attraction or repulsion between the coils and the permanent magnet, which provides a microactuation force, hence the deflection of the diaphragm.

The main advantage of using electromagnetic actuation for micropumps is the large force. Compared to electrostatic actuation, electromagnetic actuation provides a large actuation force over longer distance, and requires low operating voltage (Oh and Chong 2006). However, electromagnetic actuation requires external magnetic field usually in the form of a permanent magnet. Moreover, the electromagnetic actuation does not benefit from scaling down in size because electrostatic force reduces by the cube of scaling factor. Therefore its utilisation for microfabricated actuators is limited as only a few magnetic materials can be micromachined easily. Additionally, electromagnetic micropumps are known for high heat dissipation, and large size due to the presence of a permanent magnet and drive coil (Nisar *et al.* 2008a, Bohm *et al.* 1999).

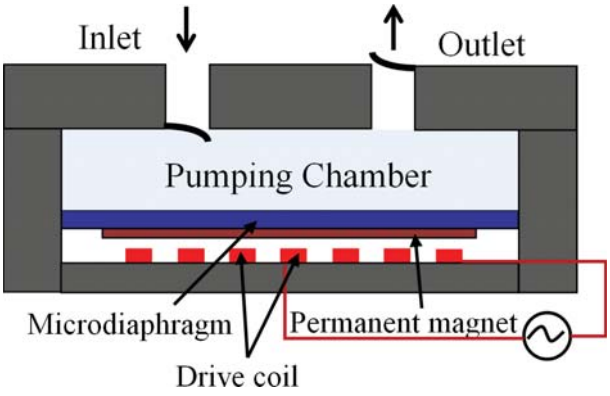

Figure 2.4. Electromagnetic micropump. Electromagnetic micropump consists of a chamber with inlet and outlet valves, a flexible diaphragm, a permanent magnet and a set of drive coils. A small current that is driven through the drive coils generates magnetic field, which creates an attraction or repulsion between the coils and the permanent magnet. This provides the microactuation force, and hence the deflection of the diaphragm.

Therefore, in relation to biomedical applications, it is apparent that the electromagnetic micropumps are not a popular choice for implants but well developed and optimised for Lab–on–a–Chip systems (Yamahata *et al.* 2005b, Pan *et al.* 2005a).

Thermo–pneumatic

As is depicted in Figure 2.5, the heating chamber of a of a thermo–pneumatic micropump is full of air inside. This air is expanded and compressed periodically using a pair of heater and cooler. The periodic change in volume of heating chamber provides the flexible diaphragm with a regular momentum to result in pumping of fluid in and out of the fluidic chamber. The pressure drop in chamber induced by volume increase, which is a function of the thermal expansion coefficient of the gas in the heating chamber (Nguyen *et al.* 2002).

It is evident that thermo–pneumatic micropumps generate large pressure and translates to large deflections and forces (Jeong and Yang 2000, Zimmermann *et al.* 2004, Schomburg *et al.* 1994). Nevertheless such micropumps suffer from high–power consumption and slow response time, which are common characteristics of thermal actuation methods.

Zdeblick and Angell (1987) reported the first thermo–pneumatic micropump, by developing a reciprocating displacement micropump with passive valves. Furthermore, a maximum flow rate of 34 μl/min was reported at low operating voltage of 6 V. Since

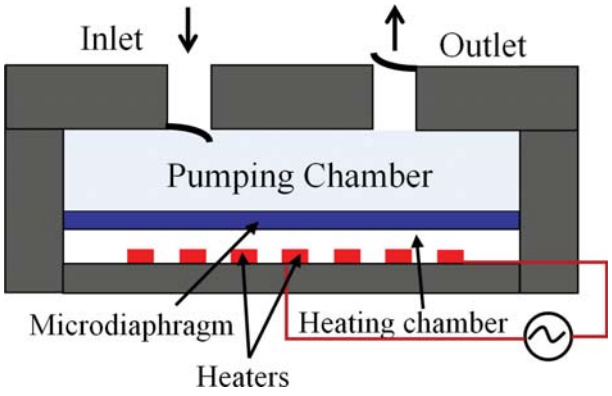

Figure 2.5. Thermo–pneumatic micropump. The actuation involves thermally induced volume change and (or phase change) of fluids sealed in a cavity with at least one compliant wall. The periodic change in volume of heating chamber provides the diaphragm with a regular momentum to result in pumping effect.

then the thermo–pneumatic actuation principle has been adopted for both drug delivery (Jeong *et al.* 2005) and Lab-on-a–Chip (LoC) applications (Kim *et al.* 2005).

Shape memory alloy (SMA)

Shape memory alloy (SMA) actuated micropumps make use of the shape memory effect in SMA materials, and the diaphragm of SMA micropumps is popularly made of Titanium/Nickel alloy (TiNi) (Benard *et al.* 1998, Xu *et al.* 2001, Shuxiang and Fukuda 2004). Being capable of restoring its original shape right after the heating/cooling cycle is the inherent useful feature of SMA (Nguyen *et al.* 2002). A conceptual design of a SMA micropump is depicted in Figire 2.6. The shape memory effect involves a phase transformation between two solid phases. SMA starts in Martensite phase and transforms into Austensite phase after being heated. This phase transformation results in shape deformation, which is utilised as an actuating force upon the diaphragm of a SMA micropump.

The advantages of SMA micropumps are, linearity retained during deflection of the diaphragm, high stress ($>$ 200MPa), and long operation cycle. Moreover, such micropumps have demonstrated low operating frequencies in the range of 1 Hz (Benard *et al.* 1997, Benard *et al.* 1998). However, the downside of SMA micropumps is considered as, the need of particular SMA materials, and relatively high power consumption. As some highlights, Benard *et al.* (1997) reported the first SMA micropump, which consisted of two TiNi membranes separated by a silicon spacer. Cantilever type check

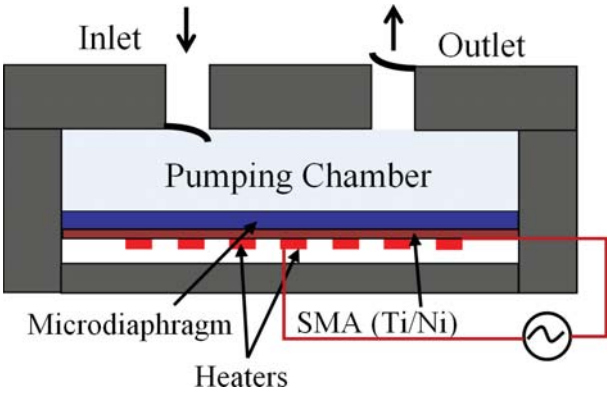

Figure 2.6. SMA micropump. The actuation is caused by a SMA alloy such as TiNi, NiTiPb, or NiTiCu, which is attached to a voltage driven microheater. As the SMA is heated, a phase transformation occurs and results in shape deformation, which is utilised as the actuating force upon the diaphragm.

valves have been fabricated for flow rectification. A maximum flow rate of 49 μl/min has been achieved at an operating frequency of 0.9 Hz, but at a high power consumption of 500 mW.

Shuxiang and Fukuda (2004) also developed a SMA actuated micropump, consisting of SMA coil, made of TiNi, and valveless diffusers for flow rectification, targeting biomedical applications. The designed micropump was able to demonstrate a flow rate of 500-7000 μl/min, and was suitable for the use in medical applications and in biotechnology such as intracavity intervention in medical practice for diagnosis and surgery.

Bimetallic

A schematic illustration of bimetallic micropump is shown in Figure 2.7. The diaphragm is made of two different metals possessing adequately discriminative thermal expansion coefficients, therefore the metals exhibit different degrees of deformation during heating, and cause the diaphragm to deflect (Zhan *et al.* 1996, Yang *et al.* 1996).

The advantages of bimetallic micropumps are limited to large force, low control voltage and simple implementation (Zhan *et al.* 1996, Zou *et al.* 1997). Furthermore, the deflection of the bimetallic diaphragm achieved is small; due to the small thermal expansion coefficients of materials involved. Although such micropumps require relatively low voltages, they are not suitable to operate at high frequencies (Oh and Chong 2006).

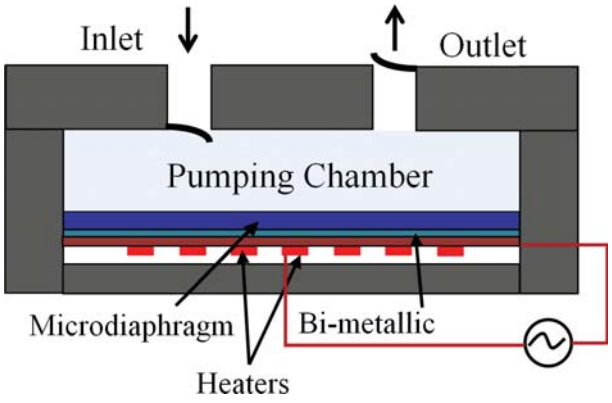

Figure 2.7. Bimetallic micropump. The deflection of the diaphragm, made of bimetallic materials, is achieved by thermal alternation as the two thermally conductive materials possess different thermal expansion coefficients.

Additionally, high temperature and complicated thermal management can be recognised as further drawbacks of bimetallic micropumps (Nguyen *et al.* 2002).

Both bimetallic and electrostatic actuation based micropump with sensing capabilities were developed by Pang *et al.* (1998), incorporating a small size membrane for actuation, for a microfluidic chip. However, based on the reported literature, it was difficult to locate any bimetallic micropumps targeted for *in–vivo* drug delivery applications, which highlights the associated restrictions of this actuation mechanism.

Ionic conductive polymer film (ICPF)

Ionic conductive polymer film (ICPF) based actuation is a novel actuation mechanism that is becoming highly popular due to its high potential in bioengineering applications. Such novel materials, mostly belonging to the electroactive polymers categories including Nafion–based ICPF, polypyrrole of conjugated polymers, and polyaniline (PANI) of conductive polymers, were investigated by researchers as possible materials for artificial muscles (Zhou and Li 2004). A schematic explaining the actuation principle of the ICPF is presented in Figure 2.8 below.

The main advantages of ICPF actuators are; low driving voltage, quick response, and most importantly biocompatibility (Nisar *et al.* 2008a, Guo *et al.* 2003). Furthermore, it can work in aqueous environments. However, the major shortcoming is its weak repeatability in batch fabrication.

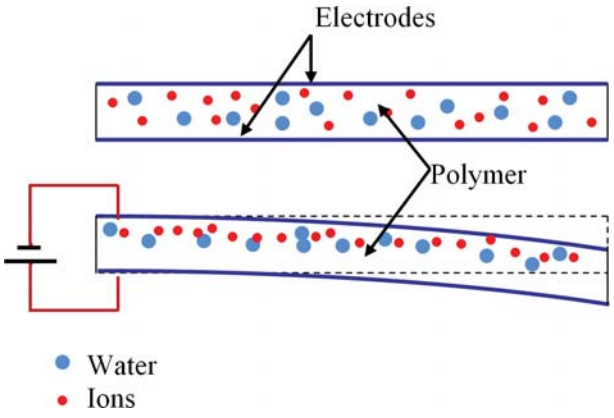

Figure 2.8. The structure of ICPF and the bending action of ICPF actuator. Once an electric field is applied, the cations in the two sides of the polymer molecule chain moves to the cathode. At the same time, each cation takes some water molecules to move towards the cathode. This ionic movement causes an expantion of the cathode and a shrinking action at the anode. With the use of an alternating voltage signal, the film can be bent alternately.

Thus far, researches have reported applications of ICPF in robotic (Guo *et al.* 2003), medical devices (Guo *et al.* 2003) and micromanipulators (Guo *et al.* 2003). Furthermore Guo and Asaka (2003) reported a successful development of a ICPF based micropump for biomedical applications. The micropump design with low power consumption (1.5 V), biocompatibility and adequate flow rate (4.5-37.8 μl/min), has potential application in medical field and biotechnology.

2.3.2 Non–Mechanical Micropumps

Non–mechanical micropumps require the conversion of non–mechanical energy to kinetic momentum, in order to supply the fluid with momentum. These phenomena are practical only in the microscale. In variation to mechanical micropumps, non–mechanical micropumps generally have neither moving parts nor microvalves. Therefore, geometry design and fabrication techniques of such micropumps are relatively simpler. However, its driving effect and performance, such as back pressure, flow rate, rise time of response and maximum deformation, are inferior, if compared with mechanical micropumps. Since early 1990s, many types of non–mechanical micropumps have been emerged and reported. Main types of non–mechanical micropumps with different actuation methods are discussed later in this section.

Magnetohydrodynamic (MHD)

Figure 2.9 depicts the schematic force fields and relations associated with magneto-hydrodynamic (MHD) micropumps. The Lorentz force is the actuation force in MHD micropumps. The force is perpendicular to both electric and magnetic fields that are provided externally (Jang and Lee 2000). MHD theory is based on the interaction of the electrically conductive fluids with a magnetic field. Moreover, the working fluid has to be chosen to have conductivity 1 S/m or higher for effective use of this actuation principle (Tsai and Sue 2007).

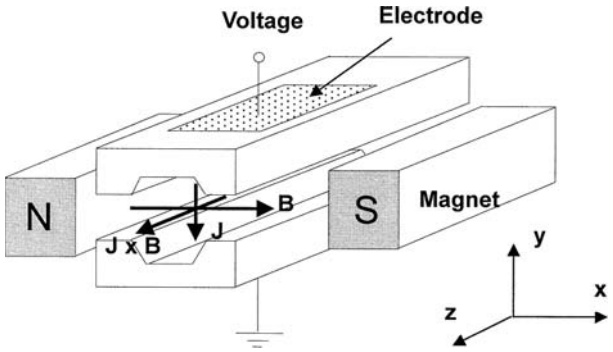

Figure 2.9. MHD micropump. The actuation principle of the MHD micropump, where driving force is Lorentz force generated in Z direction. Two external electric and magnetic fields are provided and an electrically conductive working fluid is used for pumping (Jang and Lee 2000).

The main advantage of MHD micropumps is that the ability to pump fluids with higher conductivity (Jang and Lee 2000), which greatly widens the utilisation of MHD micropumps in medical and biological applications. However, the bubbles generation due to electrolysis (ionisation) is regarded as a major drawback of MHD micropumps (Jang and Lee 2000).

The concept of MHD micropump is relatively new, and one of the first developed MHD micropumps was developed by Jang and Lee (2000), where the performance of the MHD device was investigated by varying the applied voltage from 10 – 60 V while the magnetic flux density was retained at 0.19 T. The maximum flow rate reached to 63 μl/min when driving current was retained at 1.8 mA.

Huang *et al.* (2000) presented a DC type MHD micropump targeting medicine delivery, biological and biomedical studies, with a high flow rate of 1200 μl/min at a DC control

voltage of 15 V. Such MHD micropumps are expected to be used in biomedical devices such as a drug delivery system or microfluidic propulsion application.

Electrohydrodynamic (EHD)

An electric field acting on induced charges in a fluid allows the transduction[1] of electrical to mechanical energy in an electrohydrodynamic (EHD) micropump. Therefore, the fluid flow in EHD micropump is manipulated by interaction of electric fields with the charges they induce in the fluid. In contrast to MHD micropumps, one of the requirements of EHD micropumps is that the fluid must be of low conductivity and dielectric in nature. A simple schematic of a EHD micropump and its operating principle is presented in Figure 2.10.

Figure 2.10. EHD micropump. The driving force of EHD micropump is the Coulomb force exerted on the charges between the emitter and collector electrodes, that are permeable electrodes in direct contact with the fluid to be pumped. Ions are injected from one or both electrodes into the fluid by electrochemical reactions. A pressure gradient develops between the electrodes and this leads to fluid motion between the emitter and the collector (Richter and Sandmaier 1990).

Richter and Sandmaier (1990) designed and fabricated the first DC charged injection EHD micropump, which consisted of two electrically isolated grids. An impressive flow rate of 15,000 μl/min was reported, at a large voltage of 800 V. However, it is reported that the driving voltage could be reduced by reducing the grid distance.

Even though more research has been undertaken to develop EHD micropumps (Fuhr *et al.* 1992, Darabi *et al.* 2002, Badran and Moussa 2004), a successful realisation of such a micropump for drug delivery applications is yet to be revealed.

[1] Transduction - The process whereby a transducer accepts energy in one form and gives back related energy in a different form.

Electroosmotic (EO)

Electroosmosis is one of electrokinetic phenomena, and used as a precise liquid handling technique in some microfluidic devices. As can be seen from Figure 2.11, electroosmosis phenomenon, can be used to pump electrolyte solutions. The fluid, with electric conductivity feature, is driven by appropriately exerting an external electrical field upon the channel walls that are naturally charged. As in Figure 2.11, a voltage potential is induced at the interface between the silica capillary walls and electrolyte solution.

When an ionic solution comes in contact with solid surfaces, instantaneous electrical charge is acquired by the solid surfaces. The negatively charged surface attracts the positively charged ions of the solution. If external electric field is applied at the electrodes located at the longitudinal ends of the microchannel, the thin layer of cation–rich fluid adjacent to the solid surfaces start moving towards the cathode (Nisar *et al.* 2008a, Tsai and Sue 2007). Consequently, this boundary layer like motion sets the bulk liquid into motion through viscous interaction.

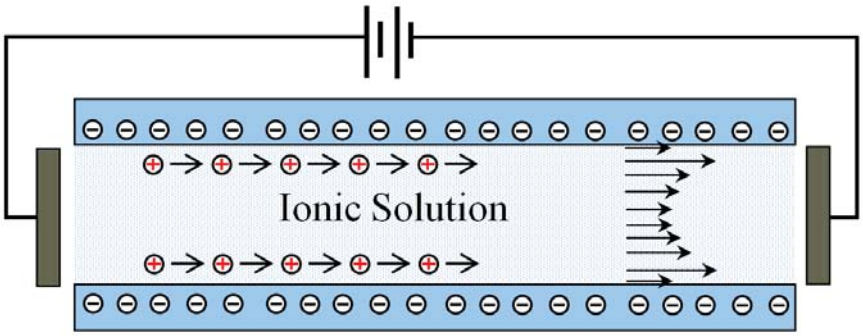

Figure 2.11. Electroosmotic micropump. Electroosmotic micropump consists of an ionic solution, solid surfaces, and two external electrodes. The ionic solution moves relative to stationary, charged surfaces when electric field is applied through external electrodes.

There are certain advantages associated with Electroosmotic (EO) micropumps. EO pumping does not involve any moving parts such as check valves, hence can be fabricated using standard and cheap MEMS techniques. Furthermore, the operation of EO micropump is quite, and flow direction is controlled by switching the direction of the external electric field. Nevertheless, major limitations of EO micropumps are requirement of high voltage for operation and electrically conductive solution.

Researchers have taken various efforts to successfully realise EO micropumps for variety of applications (Zeng *et al.* 2001, Chen and Santiago 2002, Takemori *et al.* 2005), including miniaturised fluid based systems such as micrototal analysis systems (Chen *et al.* 2005).

Electrochemical

The schematic diagram in Figure 2.12 depicts the structure and the operating principle of an electrochemical micropump. The electrochemical generation of gas bubbles by the electrolysis of water provides the driving force to dispense liquids. This is by far the most common feature of electrochemical micro pumps (Suzuki and Yoneyama 2002, Ateya *et al.* 2004).

As advantages, the design and construction of the electrochemical micropump is considered to be relatively simple and can be easily integrated with other microfluidic systems. However, the limitation of such a micropump is that the generated bubble might collapse and become water leading to unsteady and unreliable release of drug (Nisar *et al.* 2008a).

The potential of utilising electrochemical micropumps for biomedical applications were demonstrated in several occasions. As such, Suzuki and Yoneyama (2002) proposed a reversible electrochemical nano syringe pump for drug delivery, Yoshimi *et al.* (2004) developed a methodology to chemically stimulate neurons using a neurotransmitter, containing an electrochemical micropump. Furthermore, Kabata and Suzuki (2005) developed a micropump based on electrochemical principle for micro insulin injection system.

Osmotic–type

A schematic diagram of an osmotic–type micropump is presented in Figure 2.13. With an osmotic driving agent inside the chamber to provide concentration difference for working fluidic molecules across the semipermeable diaphragm, the working fluid that is outside the chamber, naturally moves towards the low density zone. Therefore, the inertia force of the moving flow directly transfers a kinetic momentum upon an actuation diaphragm (Tsai and Sue 2007).

The main advantage of osmotic–type micropump is that it does not require external power supply (mechanical or electrical) to the device. However, it suffers from low

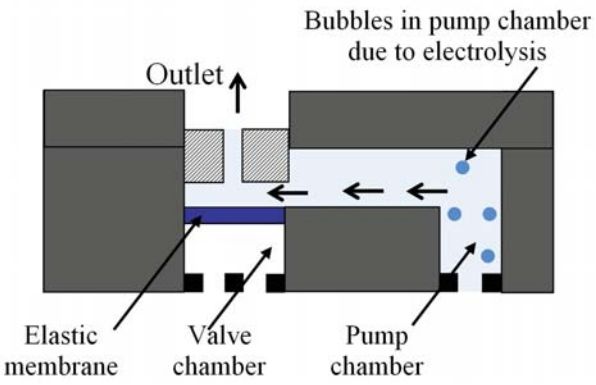

(a)

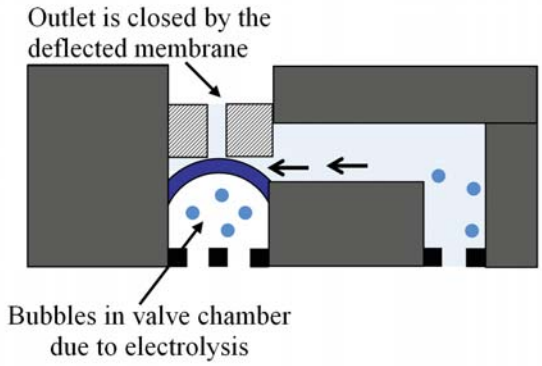

(b)

Figure 2.12. Electrochemical micropump. Electrochemical micropump consists of an elastic membrane, valve chamber, and a pump chamber. The bubble force that is generated by electrochemical reaction during electrolysis is utilised as the driving force. (a) Demonstrate the on state of the pump, and (b) the off state of the pump.

flow rate, low response with long time delay, and the semi–permeable diaphragm might depart from the substrate after a certain period of time (Su *et al.* 2002, Su and Lin 2004). These drawbacks limit its implementation in biomedical applications.

Su *et al.* (2002) as well as Su and Lin (2004) presented water–powered osmotic type micropumps for drug delivery systems. However, these designs suffer from the above mentioned limitations, and hence restrict their use in most bio–chips.

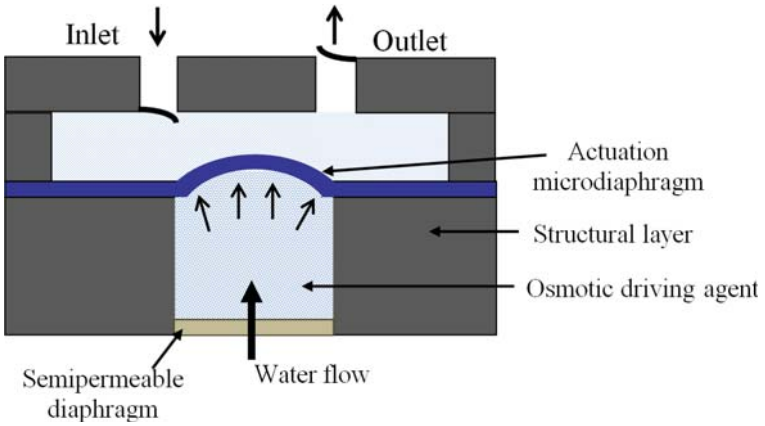

Figure 2.13. Osmotic–type micropump. Osmotic–type micropump consist of actuation diaphragm, semipermeable diaphragm, osmotic driving agent and other necessary components such as microvalves and fluidic chamber.

Electrowetting (EW)

In electrowetting (EW), wettability change due to applied electric potential. The fluid is transported using surface tension, which is an interfacial force that dominates at microscale. When a voltage is applied on the dielectric layer, this results in decreasing the interfacial energy of the solid and liquid surface, leading to fluid flow.

Furthermore, continuous EW is generally applied to adjust the surface tension between two immiscible liquids such as liquid–phased metal (mercury) and electrolyte (Tsai and Sue 2007). As depicted in Figure 2.14, the interface between the liquids is referred to as electric double layer (EDL). As a result of protonation effect on the mercury surface, the electric potential between right end of mercury droplet and the cathode of electrode pair becomes higher than the counter electric potential on the left side. Therefore, a surface tension difference beside a mercury droplet pushes the droplet toward right.

The advantages of continuous EW are, there is no involvement of heating of the liquid, faster speed, and low power consumption.

Yun *et al.* (2002) reported a continuous EW micropump with attractive attributes such as flow rates up to 70 μl/min, low driving voltage of 2.3 V, and low power consumption of 170 μW. However, its targeted applications were not mentioned.

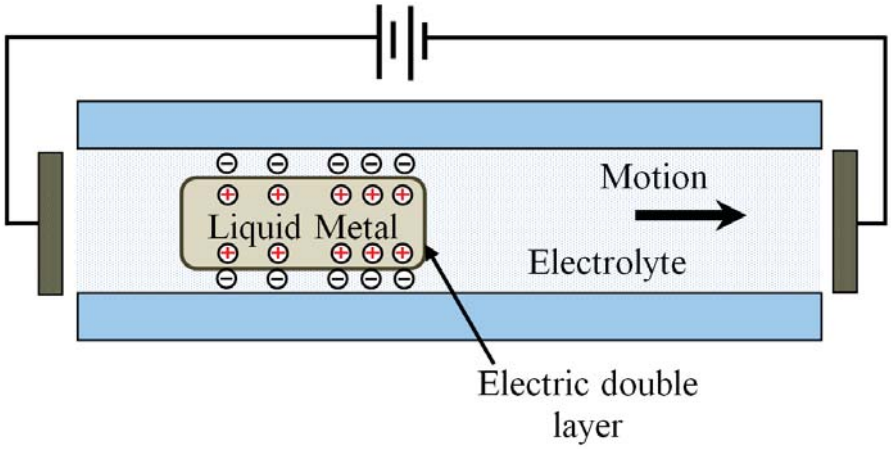

Figure 2.14. Electrowetting micropump. Continuous EW is applied to adjust the surface tension between two immiscible liquids such as liquid–phased metal (mercury) and electrolyte (Tsai and Sue 2007). Due to the protonation effect, an electric potential difference take place beside the EDL, and the resulting surface tension difference pushes the mercury droplet toward right.

Bubble–type Micropump

As can be seen in the schematic illustration in Figure 2.15, the pumping effect in bubble type micropumps is based on the periodic expansion and collapse of bubble generated in microchannel. The bubbles are periodically generated by a heat process, which is controlled by an input voltage.

If the heating process is not preferred or allowed, the application scope of such micropumps is limited, as bubble micropumps always need to be heated to generate the required actuation (Tsai and Sue 2007). Also Zahn *et al.* (2004) reported microneedles integrated with an on–chip MEMS bubble micropump for continuous drug delivery applications, such as to monitor glucose levels for diabetes patients. Various researchers have also demonstrated the operation of valveless, bubble type micropumps that were based on diffuser/nozzle elements as flow rectifiers (Tsai and Lin 2001, Jung and Kwak 2007). The recorded flow rates were between 5–8 μl/min, which required high power input in some instances (Tsai and Lin 2001).

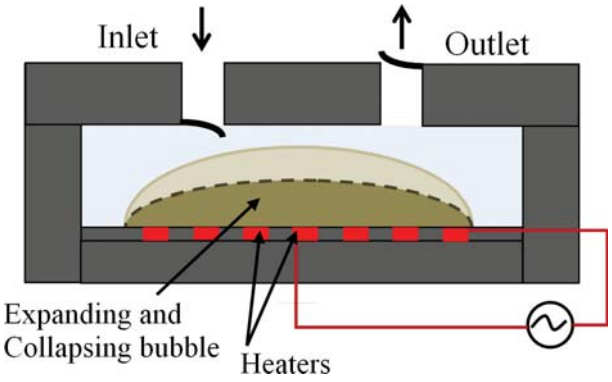

Figure 2.15. Bubble–type micropump. Bubble–type micropump consists of a expanding and collapsing bubble, microheaters, pumping chamber and microvalves. The pumping mechanism is due to growth and subsequent collapse of the bubble, which is nucleated on the microheaters embedded in the bottom layer of the pumping chamber.

Flexural Planar Wave (FPW)

Ultrasonic principle based Flexural Planar/Plate Wave (FPW) is a gentle micropump principle with no moving parts or heat, and strong electric field involved. The ultrasonic micropump effect is caused by the acoustic streaming, which is induced by a mechanical travelling wave. As can be seen from Figure 2.16, the mechanical wave can be a FPW, or a Surface Acoustic Wave (SAW). The mechanical waves are excited by Inter Digital Transducers (IDT) placed on a thin piezoelectric membrane (substrate) or on a piezoelectric bulk material. The micropump has a thin microchannel, and therefore also suitable for multi phase based, particle separation applications. Furthermore, using curved IDTs instead of the standard pattern, locally sample concentration can be achieved with this kind of pump.

The main advantages of ultrasonic micropumps are the very low power requirement for fluid pumping and the ability to easily reverse the pumping direction. Furthermore, in contrast to the EHD micropumps, there is no such limitation on the conductivity of liquids or gases in FPW micropumps (Nisar *et al.* 2008a). However, the strength of the mechanical traveling wave (propagating SAW mode) may be dampened by the pumping fluid, since the fluid is in direct contact with the mechanical traveling wave.

Several investigations were reported regarding ultrasonic pumping effects, utilising piezoelectric plates such as ZnO and PZT (Moroney *et al.* 1991a, Luginbuhl *et al.* 1997, Nguyen *et al.* 2000a, Meng *et al.* 2000). Here, Luginbuhl *et al.* (1997) reported a dual transducer patterned ultrasonic micropump. In this approach, the fluid motion was

demonstrated when ultrasonic flexural waves propagated in a thin microdiaphragm. Nguyen *et al.* (2000a) also proposed microfluidic system based on FPW micropump. The FPW micropump required low operating voltage and less power consumption (less than 10 mW). Their proposed micropump was suitable for delivering sensitive biomaterials. Furthermore, potential applications also included cell manipulating and drug delivery systems.

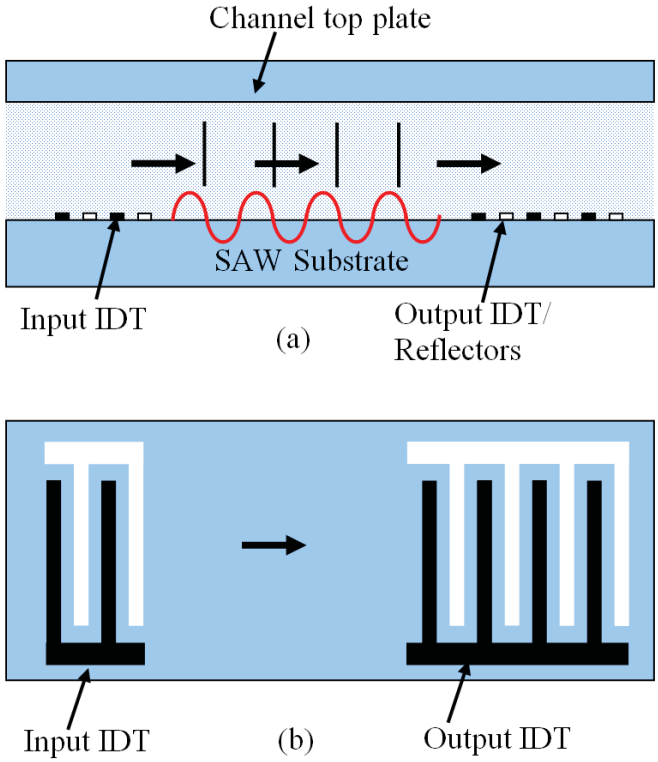

Figure 2.16. Ultrasonic micropump. The mechanical waves are excited by Inter Digital Transducers (IDTs) that are placed on a thin piezoelectric membrane or on a piezoelectric bulk material. When an ultrasonic control signal is applied at the input IDT, the mechanical stress waves are excited, and energy from these waves are transferred to the fluid in contact, hence pumping action is initiated.

Meng *et al.* (2000) also reported a micromachined micropump using ultrasonic FPW, where a mechanical wave was travelling along a thin membrane to excite an acoustic field in the fluid that is in contact with the membrane. Bidirectional and focused flow was achieved by a novel combination of radial transducer patterns. Potential applications of this type of micropumps include micrototal analysis systems and drug delivery devices.

2.3.3 Application Specific Suitability of Micropumps

As described above and in previous micropump reviews (Nguyen *et al.* 2002, Razzacki *et al.* 2004, Ziaie *et al.* 2004, Squires and Quake 2005, Tsai and Sue 2007, Iverson and Garimella 2008), a wide variety of possible pumping mechanisms have been proposed for the emerging needs in microscale flows. As pump sizes have been reduced to the micro domain, the effect of centrifugal and inertial forces are generally limited. The large surface–to–volume ratio instead amplify the effects of viscous forces, often making them the dominant force. Additionally, the force per unit volume of some pumping techniques actually increases with reduction in length scale. In this section, various pumping technologies that were reviewed are briefly compared qualitatively and quantitatively, especially with respect to a biomedical applications.

The use of MEMS–based micropumps for various biomedical applications such as *in-vivo* drug delivery, transdermal insulin delivery, artificial sphincter prosthesis, antithrombogenic micropumps for blood transportation, injection of glucose for diabetes patients and administration of neurotransmitters to neurons, and chemical and biological sensing have been reported.

In view of the increased use of MEMS–based micropumps in implantable drug delivery systems and emphasis on lowering the manufacturing costs, silicon is now being replaced with polymer based materials such as polydimethylsiloxane (PDMS) and polymethylmethacrylate (PMMA). The use of polymer based materials is rapidly growing because of their good biocompatibility, excellent physical and mechanical properties, low cost simple structure and fast fabrication.

In selecting a suitable actuation mechanism, and hence a pumping technology, various factors other than pressure and flow rate are need to be considered. As such, the amplitude of the applied control voltage required for these micropumps is one of the important factors which varies widely and can be compared directly. The control voltage determines the required electronics and other components to operate these micropumps.

Based on the presented literature review and other extensive reviews (Nguyen *et al.* 2002, Razzacki *et al.* 2004, Ziaie *et al.* 2004, Squires and Quake 2005, Tsai and Sue 2007, Iverson and Garimella 2008), electrostatic, piezoelectric and thermopneumatic micropumps are known to produce higher flow rates at the expense of high–applied voltage values. Furthermore, micropumps with conducting polymer film actuators such as

ICPF appear to be the most promising mechanical micropumps which provide adequate flow rates at very low applied voltage. Bimetallic micropumps also recognised for their higher flow rates at a lesser control voltage.

Non–mechanical micropumps are also dependent on various other factors in addition to pressure and flow rate. MHD and EHD micropumps are known to produce high flow rates at the expense of high operating voltages. Electroosmotic micropumps require high operating voltages and produce low flow rates. Furthermore, electroosmotic micropumps are generally used in microanalysis systems where low flow rates are required. Whereas, electrowetting and electrochemical type of micropump are the most promising ones which exhibit high flow rate at low applied voltage.

In contrast to mechanical micropumps, working fluid properties influence the flow rates and must be taken into account when choosing non–mechanical micropumps. It is known that electroosmotic and magnetohydrodynamic micropumps can handle many working fluids which are widely used in chemical and biological analysis. Moreover, electrochemical micropumps can also handle a variety of solutions such as insulin and neurotransmitter solution in drug delivery application.

As with flow rate, size of the micropump is a highly important physical parameter as it greatly influences the *in–vivo* application of a micropump. However, with integration of extra microcomponents onto generic micropumps, to develop smart MEMS devices, the miniaturisation is a challenge.

Based on the extensive literature review, it can be concluded that overall commercialisation of MEMS micropumps in total drug delivery systems and other biomedical applications is still in its early stages and growing rapidly. A vast amount of technical information is available for a number of micropump concepts. However, many of the novel micropumps reported in literature for drug delivery applications still need to be incorporated onto practical devices.

It is evident that deciding a suitable micropump for a particular biomedical application is a challenge, and therefore, this will continue to motivate researchers to work on developing micropumps and incorporating them in *iv–vivo* drug delivery systems.

2.4 Microvalves for Flow Rectification

In order to obtain flow rectification from the oscillatory motion of the diaphragm, valves are incorporated into the design of diaphragm based micropumps. Valves take many forms and can feature passive or active control. Although a relatively older concept, diffuser/nozzle type fixed–geometry valves have been investigated in the recent past for specific applications such as drug delivery as they employ no moving parts (Cui *et al.* 2007, Cui *et al.* 2008). Recently, attractive modifications to the standard diffuser/nozzle valves that accommodate regions of vortex circulation that is similar to Tesla valves, have been studied for use with diaphragms based micropumps (Izzo *et al.* 2007). Microvalves are used to convert the non–directional flow to directional flow. As presented in Figure 2.17, microvalves can be classified into dynamic and static geometry categories, and further divided into active or passive sub-categories (Iverson and Garimella 2008). In this review, valveless micropumps refer to micropumps with no moving parts for flow rectification, but with static or fixed–geometry valves.

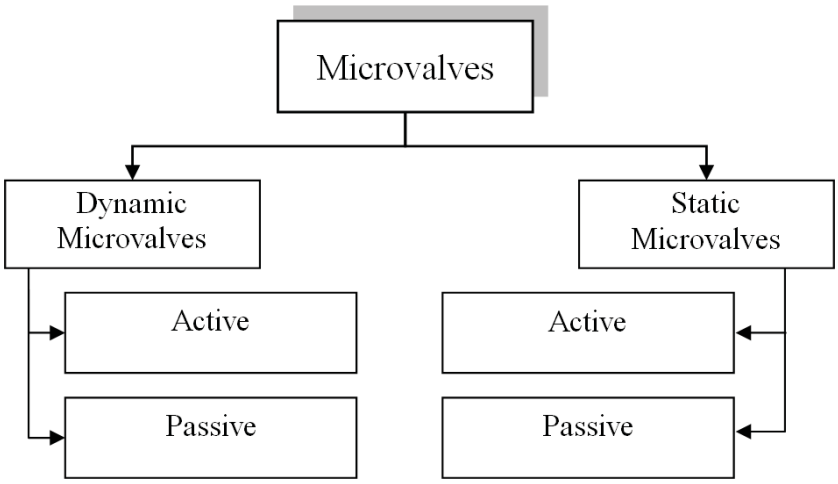

Figure 2.17. Microvalve Classification. Different types of dynamic and static microvalves.

2.4.1 Dynamic Microvalves

Dynamic–geometry microvalves can be defined as structures that provide flow direction by deformation, motion or deflection. Moreover, active microvalves require energy such as electrical or thermal, for flow rectification. Figure 2.18 depicts a generic schematic of a dynamic, active microvalve. Therefore, it should be noted that, almost

any of the actuation mechanisms discussed under Section 2.3.1 can be used as an active, dynamic microvalve. Cantilever structures and thermally responsive valves are some of the examples that represent active dynamic microvalves (Woias 2005, Samel *et al.* 2007). Dynamic–geometry microvalves can also be passive in that they require no energy for activation. PDMS based flexible cantilever structures have been used extensively as a dynamic, passive valve. Valve designs for these flap structures differ when considering low and high Reynolds number flows. Therefore, care is needed in fabricating PDMS based valves to prevent any possible stiction (Loverich *et al.* 2007).

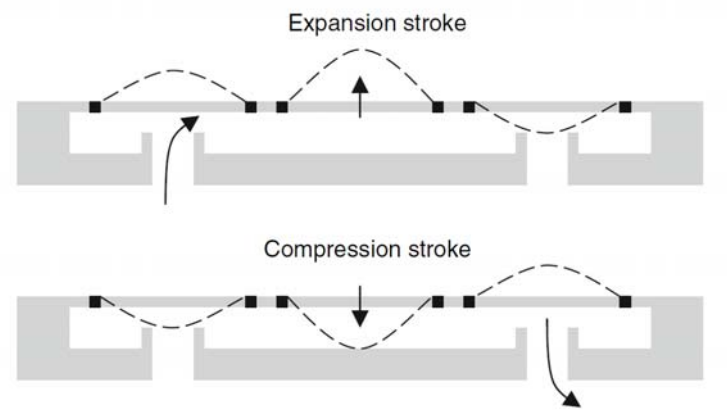

Figure 2.18. Dynamic and active diaphragm microvalves. Generic representation of a dynamic, active diaphragm based microvalve. These microvalves operate to generate a directional flow, by opening and closing in synchronous with the diaphragm vibration such that the pump chamber outlet is closed before the expansion stroke and the pump chamber inlet is closed before the compression stroke (Iverson and Garimella 2008).

Despite the difficulties in combining with classical 2D microfabrication techniques, ball valves have been successfully implemented by various researches (Pan *et al.* 2005b, Yamahata *et al.* 2005a). The disadvantages of dynamic–geometry valves include the risk of fatigue failure in long–life operation, stiction, and requirement of a longer response time for activation. However, since dynamic–geometry valves commonly provide a physical barrier to reverse fluid flow, they often can withstand large–back pressures.

2.4.2 Static Microvalves

Static–geometry microvalves employ no moving parts or boundaries for flow rectification. The geometry is fixed and the conversion of non–directional flow into directional

flow occurs through the addition of energy (active) or through geometries in which the desired flow behavior is induced by fluid inertia (passive). Based on the published literature (Olsson 1998, Rosa and Pinho 2006, Olsson *et al.* 2000, Izzo *et al.* 2007), it is evident that static–geometry valves have been extensively used due to the simplicity of their design and the low risk of failure.

Among the static–geometry microvalves that are actively controlled, laser–induced heating (Baroud *et al.* 2005), and thermally controlled, viscosity–based valves have been investigated in vibrating diaphragm pumps, where the rectification principle is based on the temperature dependence of liquid viscosity, which causes a variation in flow resistance (Matsumoto *et al.* 1999). A structure of a micropump with viscosity–based valves is illustrated in Figure 2.19 (a).

Moreover, static–geometry based passive microvalves rely on the geometry itself to produce directional flow. As can be seen from Figure 2.19, the two most common types are diffuser/nozzle and Tesla valves. These microvalves are very attractive since there are no moving parts and they require no additional energy for operation. Hence, less likely to fail.

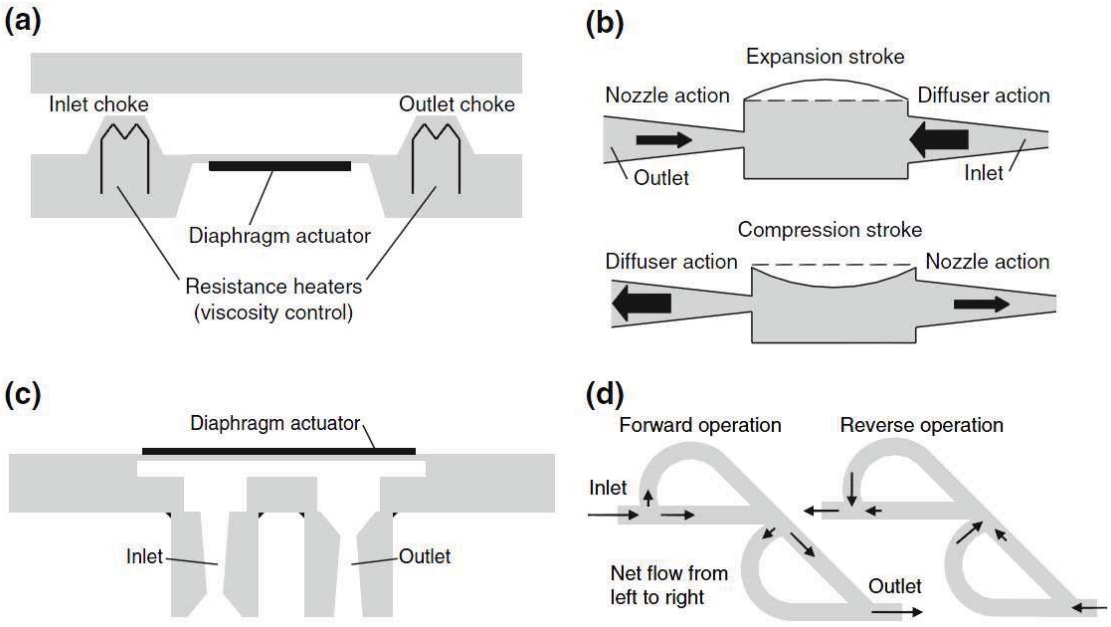

Figure 2.19. Static and fixed–geometry microvalves. (a) Thermally controlled viscosity valve, (b) Horizontal diffuser/nozzle valve, (c) Vertical diffuser/nozzle valve, and (d) Tesla valve (Iverson and Garimella 2008).

The diffuser/nozzle concept was first presented by Stemme and Stemme (1993), and importantly the use of such microvalves in low Reynolds number flows were studied by (Singhal *et al.* 2004), where the ability to rectify flow for laminar flows with the larger rectification occurring at higher Reynolds numbers were demonstrated.

Additionally, Tesla valves are bifurcated channels in which the separated flow re–enters the main flow channel perpendicularly when the flow is in the reverse direction (Izzo *et al.* 2007, Iverson and Garimella 2008). This concept was first presented by Tesla (1920), and has been used in many micropump designs since then.

Apart from the standard implementation of the above valves, it is been reported that researchers have also investigated a combination of diffuser/nozzle and Tesla type valves (Izzo *et al.* 2007). Specifically, regions for vortex circulation have been added along the sides of the diffuser/nozzle regions for more efficient flow rectification.

Based on this presented information, it is evident that there are a number of considerations in selecting a microvalve type for a specific application. Especially, for *in–vivo* biomedical applications, it is necessary to consider whether the potential advantage in flow rectification for actively powered microvalves is worth the added complexity and power consumption over that for passive microvalves. The absence of moving parts from the fixed–geometry microvalves are considered to be advantageous when the fluid contains cells or other materials that may clog. Moreover, the wear and fatigue issues are eliminated in contrast to dynamic microvalves.

2.5 SAW Devices for Wireless and Secure Interrogation

2.5.1 Surface Acoustic Wave (SAW) Devices

Surface Acoustic Wave (SAW) devices are widely used in MEMS applications, which require secure, wireless, and passive interrogation (Jones *et al.* 2008). These devices are recognised for their versatility and efficiency in controlling and processing electrical signals. They are based on propagation of acoustic waves in elastic solids and the coupling of these waves to electric charge signals via an input and an output Inter Digital Transducers (IDT) that are deposited on the piezoelectric substrate. As shown in Figure 2.20, a SAW device consisting of a solid substrate with input and output IDTs (Jones *et al.* 2008). An IDT is an array of narrow and parallel electrodes connected alternately to two bus bars made out of thin–film metal. The purpose of placing a set

of IDTs on a SAW device is to provide a coupling between the electrical signal received (or transmitted) and the mechanical actuation of the piezoelectric substrate material. Since SAW devices are mostly used for wireless applications, a micro–antenna is need to be attached to the input IDT.

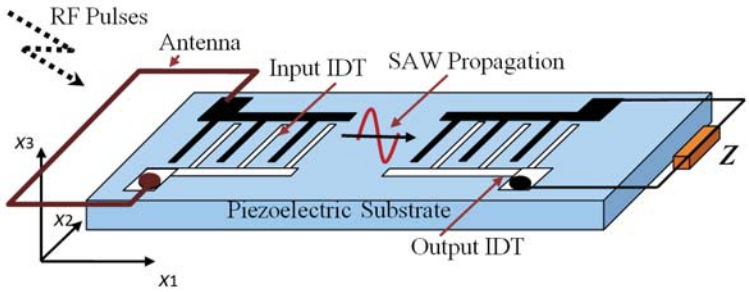

Figure 2.20. SAW device. Standard SAW device consist of a piezoelectric substrate, input IDT, and an output IDT. Input IDT is connected to a micro-antenna for wireless communication, and a load is connected to the output IDT for measurements.

Acoustic waves in these devices are propagating as surface waves, and hence can be perturbed easily by modifications to the substrate surface. Such features have enabled a large number of resonant sensors for applications such as chemical sensors (Ruppel *et al.* 2002), gyroscopes (Varadan and Varadan 2000), and accelerometers (Subramanian *et al.* 1997). SAW devices also find application in oscillators, pulse compressors, convolvers, correlators, multiplexers and demultiplexers (Ruppel *et al.* 2002).

2.5.2 SAW based Wireless Communication–Current Technology

SAW devices have become an indispensable part of the modern electronic communication industry, due to their usefulness as IF, RF, and GPS filters for various applications. It has been reported that SAW devices, as front–end filters for GSM–900, can withstand power levels more than 34 dBm, and in the 2 GHz range (GSM-1800, GSM-1900, UMTS); power levels up to 30 dBm, with the availability of new electrode materials (Ruppel *et al.* 2002). This means that SAW RF filters can handle all power levels used in the terminals of today's mobile communications systems.

Over the years, SAW devices are known to offer superior performance, due to a range of factors such as high stability, excellent aging properties, low insertion attenuation,

high stopband rejection (processing gain), and narrow transition width from passband to the stopband (Ruppel *et al.* 2002).

Therefore, it is evident that SAW based wireless communication is a well established field in RF–MEMS and Bio–MEMS devices, and has a great potential to incorporate with modern biological implants. As presented in the proceeding section, this attractive low–powered interrogation mechanism can be further improved by incorporating a secure code onto the SAW device, by means of coding the IDT pattern.

2.5.3 SAW based Wireless Communication with Security

In implantable drug delivery applications, it is important that the device to be securely operated, and not to be triggered by spurious RF signals. After considering the aforementioned advantages in SAW communication, a SAW correlator is an ideal choice to incorporate the secure interrogation of the device (Tikka *et al.* 2007, Tikka *et al.* 2008). As depicted in Figure 2.21, SAW correlator consists of a coded IDT to ensure that the device responds only to a matched RF signal (Jones *et al.* 2008, Tikka *et al.* 2008). In a SAW correlator, an acoustic wave is propagated with a high processing gain, only if the coded IDT pattern is identical to the code sent through the interrogating signal. The code can take the form of either a delay line or a resonator configuration (Schmidt *et al.* 1996).

Importantly, due to the low velocity of SAWs, long delay times in the range of some microseconds can be achieved using rather small SAW chips. Therefore, at VHF/UHF frequencies, environmental echoes caused by electromagnetic multipath propagation phenomena are safely faded away, even before the SAW signal is compared against the coded IDT geometry. Therefore, the coded SAW signal can easily be separated from environmental echoes in the time–domain (Schmidt *et al.* 1996). This is a great add on that exist in SAW–based wireless interrogators, compared to other radio link systems.

The operation of the coded SAW device (correlator) is as follows. The acoustic wave propagation in a correlator can be facilitated by designing the IDT fingers in such a way, so that their polarity and orientation is related to the input code in the receiving RF signal. As a result, the code used in the interrogating RF signal need to be equivalent to the finger pair configuration embedded in the correlator. When a matched

code is feed to the correlator, an acoustic wave with same sign and phase is generated and the interact constructively to generate a signal with a high processing gain. However, if an incorrect code is input to the system, the generated pulses will interact destructively (Jones *et al.* 2008). Therefore, by using a longer code (hence increasing the number of finger pairs) it is possible to increase the number of unique combinations of control signals. Overall, this enhance the security feature of the device by making it harder to manipulate or abuse its activation code.

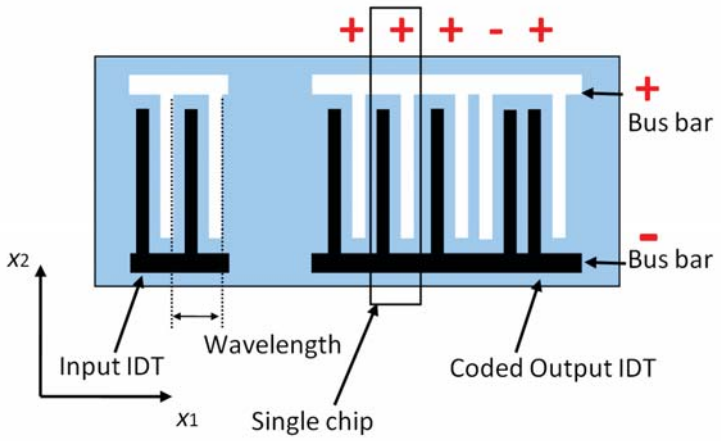

Figure 2.21. Basic structure of a SAW correlator. The output IDT geometry determines the code of the generated acoustic wave. A 5–bit Barker sequence $(+++-+)$ is encoded in to output IDT. Referring to the highlighted finger pair, the charge on the first finger creates a negative acoustic pulse and the charge on the second finger creates a positive pulse, hence creating an overall positive pulse. Fourth finger pair is connected to the busbar with an opposite sign to the highlighted pair, which generates an overall negative pulse. By ordering the fingers in certain ways it is possible to control the creation of acoustic pulses. This effect is exploited in coding the devices for secure actuation.

It is worth noting that the energy received from the receiver antenna is transduced to the input IDT, and through the SAW mechanism to the output IDT, since the critical signal comparison is taken place at the output IDT.

2.6 Proposed Interrogation Methodology

The proposed interrogation mechanism in this thesis is therefore a novel combination of two well established SAW based technologies; one is for RF communication and the other is for the incorporation of secure interrogation.

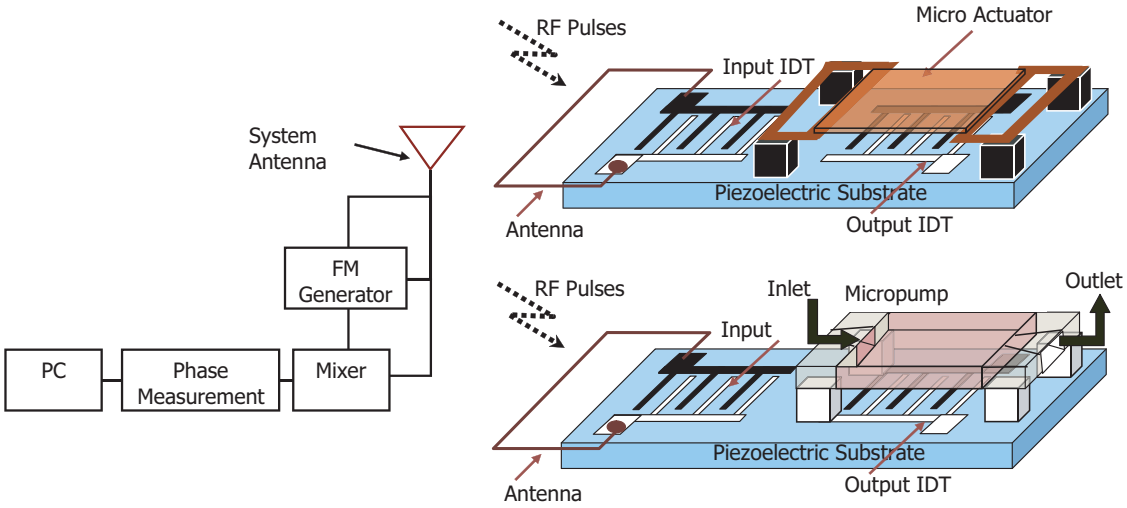

Figure 2.22. SAW based wireless interrogation of a microactuator and a micropump. The microactuator and micropump structure is placed on top of the output IDT of a SAW device, separated by a thin air–gap. SAW device consist of a piezoelectric substrate, input IDT, and output IDT. Input IDT is connected to a micro-antenna for wireless communication. A a SAW correlator can be used for secure actuation.

The ability to store energy in SAW, and the possibility of handling high frequencies enables the construction of passive, low–cost devices for wireless communication with the capability to be interrogated by RF signals (Hamsch 2004). Moreover, as is elaborated in Section 2.5.3, by using a SAW correlator instead of a standard SAW device, the security feature can be incorporated into the wireless interrogation, with no active electronics being added to the device.

Figure 2.22 depicts a concept drawing, illustrating the implementation of the proposed mechanism to securely interrogate and actuate microactuators and micropumps. For micro scale actuations, a conductive plate (or diaphragm) is placed on top of the output IDT, with a separation of few micrometers, using an air–gap. In the arrival of a matched code at the output IDT, a low–powered electrostatic actuation force is generated on the plate (diaphragm), causing micro deformations in the conductive plate.

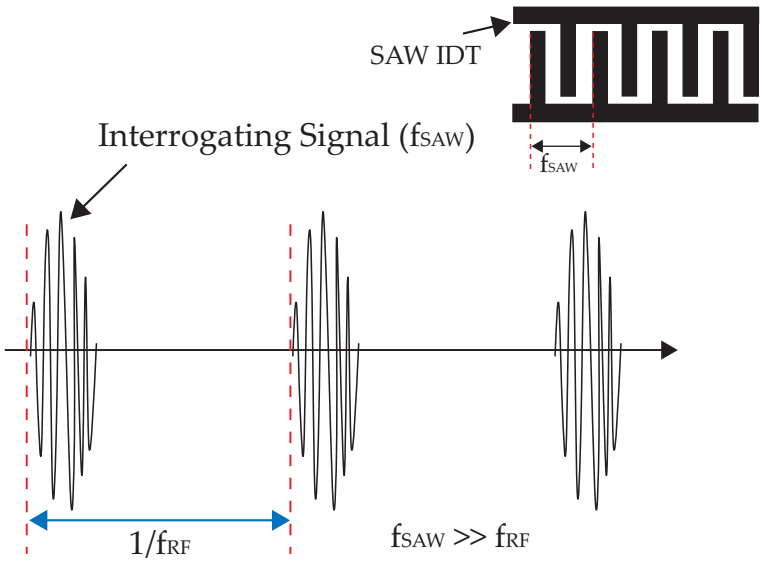

Figure 2.23. The relationship between the SAW frequency and the trigger frequency of interrogating signal. The SAW frequency (f_{SAW}) is determined by the IDT finger pattern. The trigger frequency of the interrogating signal (f_{RF}) is a very much scaled down value, compared to f_{SAW}.

A typical SAW device operates at a high frequency, which is much larger than few Mega Hertz (MHz). As can be seen from Figure 2.23, in order prevent high frequency vibrations of the proposed microactuator and microdiaphragm, the trigger frequency of the interrogating signal (f_{RF}) is selected to be a very much scaled down value, compared to the actual SAW frequency (f_{SAW}). Therefore, $f_{RF} \ll f_{SAW}$, and hence the oscillating frequency of the electrostatic field also become smaller compared to the SAW frequency (Hertz range).

This batteryless, and low powered innovative actuation mechanism is adopted in this research and further illustrated and extensively investigated in Chapters 3 and 4 and also implemented in Chapter 6.

2.7 Potential Biomedical Applications

2.7.1 Potential Drug Delivery Applications

The proposed transcutaneous micropump can be utilised for site specific drug dosing for various applications such as Hyptertension control, cancer treatments, and diabetes control. Here, a brief analysis is presented, highlighting the potential use of the proposed micropump in controlling hypertension.

Drug Delivery for Hypertension

High blood pressure, also called hypertension, is elevated blood pressure in the arteries. Hypertension results from two major factors, which can be present independently or together; (i) the heart pumps blood with excessive force, and (ii) the body's smaller blood vessels (arterioles) become narrow, so that blood flow exerts more pressure against the vessels' walls.

It is been reported that hypertension places stress on several organs (target organs), including the kidneys, eyes, and heart, by causing them to deteriorate in functionality over time. Furthermore, it is been reported that high blood pressure contributes to 75% of all strokes and heart attacks (Lifespan 2009).

In addition to lifestyle and dietary changes, various types of drugs are available as a major treatment for hypertension. Some of the commonly used anti–hypertensive medications are listed in Table 2.1. In some situations targeted quick delivery of correct amount of drug would make a difference between life and death for a patient.

Therefore, based on the novel features associated with the proposed micropump, it could be implemented to facilitate a targeted and effective delivery of commonly used anti–hypertensive drugs, especially the ones that block specific type of hormone receptors.

2.7.2 Other Potential Applications

In addition to drug delivery, this proposed MEMS device and RF secure communication technology could be implemented in a range of other applications. As such; contraception for men, ultra fast DNA sequencing, flow cytometry, Lab–on–a–Chip (LoC) applications, and micromixing, as well as non–biomedical applications such as

Table 2.1. Commonly used anti–hypertensive drugs. These medications mainly block specific type of hormone receptors to control hypertension, hence a range of other disorders (Lifespan 2009).

fuel cell design, structural health monitoring and ink jet printer head modelling. Here, a brief illustration is presented highlighting the implementation of SAW based secure microactuation principle in relation to contraception for men.

Contraception for Men

The SAW based microactuator approach that was proposed in Section 2.6 (also further investigated in Chapter 3) can be extended to introduce a novel and innovative approach to prevent unintended pregnancy, by implementing a non–hormonal contraceptive method for men, by means of implanting a SAW device based, secure microvalve through the *vas deferens*, which interferes and prevents sperm delivery. Such a microvalve would incorporate highly relevant features such as wireless control, batteryless operation, small size and mass, biocompatibility with no active electronics, low cost fabrication, and increased reliability.

One of the key novelties of such a contraceptive device is that coded RF energy is transduced directly to perform mechanical actuation, only when the implanted code matches the code in the interrogation signal. Therefore, this innovation can successfully eliminate the requirement of a battery and active electronics to go with the microvalve, hence the microvalve can be substantially miniaturised to implant through the *vas deferens*, without any requirement of subsequent surgery to replace power sources.

This type of contraceptive device could be much more attractive compared to the current male contraception approaches and developments such as vasectomy, implants that cause permeant occlusion (Intra Vas Device-IVD), and hormones injections, due to a host of features. As such the this novel microvalve is non–occlusive and electronically reversible, requires only once-off surgery to implant, and specifically designed to be remotely and securely interrogated at close proximity, with great protection against spurious signals.

Furthermore, because of the easily and safely reversible nature of the microvalve, this methodology is immune to common side effects such as the generation of enhanced antibodies that destroy sperms, and the reduction of fertility due to back pressure caused by permanent blocking, that exist in current methods (Pitz *et al.* 2002).

2.8 Chapter Summary

The preceding sections in this Chapter provided a detailed review of MEMS based micropumps and their actuation mechanisms in recognising the significance of such micropumps for *in–vivo* micro drug delivery applications. Various types of mechanical and non-mechanical micropumps and their suitability for biomedical applications were highlighted. Micropump actuation mechanisms, their size and mass, and flow rates are some of the critical parameters that were highlighted in the review.

Furthermore, a comprehensive review of microvalves was also presented and their advantages and limitations were discussed. The important features associated with static–geometry based, passive, diffuser/nozzle elements found to be an attractive, low cost solution for flow rectification.

In addition, this Chapter introduced a SAW device based novel interrogation mechanism, as the driving technology for a wirelessly operated, securely actuated microactuators and micropumps that are designed for biomedical implants such as micro drug delivery. Furthermore, some of the potential applications of this micropump were also discussed.

The existence of well known, SAW based, communication and interrogation technologies were briefly reviewed. Consequently, the novel actuation mechanism was introduced. In Chapter 3, the actuation mechanism is extensively investigated in the context of SAW based actuators, and then extended to SAW based microdiaphragms in Chapter 4.

Chapter 3

Electrostatic Microactuator Design

INCREASING demand for wireless and low power operated MEMS devices for biomedical applications highlight the requirement of wirelessly interrogated micro devices. The novel SAW based actuation mechanism that was proposed in Chapter 2 is implemented in this chapter. Detailed theoretical analysis explaining how the entire SAW device based actuator operation is carried out, and boundary conditions applicable for presented design is used to derive the electric potential wave forms, and hence the electrostatic field between the SAW device and the conductive plate. Displacement analysis of the conductive actuator is obtained. Rayleigh–Ritz method based analytical model is carried out to investigate the steady state behaviour of the microactuator. Then static analysis results are generated using ANSYS simulation tool and compared with the theoretical results obtained by Rayleigh–Ritz method.

Once the static analysis was completed, the dynamic behaviour of the SAW device based electrostatic actuator was studied using transient analysis. This is more substantial in investigating the operating frequency of the conductive plate. Because of the time varying electrostatic field, it was found that the oscillating frequency of the actuator is much less than that of the SAW frequency.

3.1 Introduction

Actuators are one of the important components in microvalves and micropumps for fluid manipulation. The design of a suitable actuator device to pump the fluid at the microscale, for accurate operation, is of great importance. As reviewed in Chapter 2, many types of microactuators have been developed to match different requirements for various applications (Tsai and Sue 2007, Varadan and Varadan 2000). With miniaturisation, physical scaling laws inherently favour some technologies and phenomena over others. In some cases, technologies that can be made by micromachining work well at the microscopic scale, but have no analogy or usefulness in the macroscopic scale. Moreover most of these actuators are too complicated to fabricate within a micropump structure.

Notably, SAW devices are used to develop micromachines such as ultrasonic micromotors and fluid transfer methodologies such as flexural micropumps (Wixforth 2003, Strobl *et al.* 2004). Currently available microfabrication technologies such as photolithography and X–ray lithography with a combination of other processes have enabled the use of SAW devices for a variety of self–contained MEMS applications, which have advanced functionality and performance. The key benefits of these micromachines are; their small size, ease of production, and low–cost. As highlighted in Chapter 2, the use of SAW devices for micro actuation applications provides the great benefit of controlling and interrogation of devices remotely, without direct physical user intervention (Dissanayake *et al.* 2007, Varadan and Varadan 2000, Jones *et al.* 2008).

In this chapter, SAW based electrostatic actuator modelling is discussed. Consequently such a microactuator can be embedded in a microfluidic device to modulate the fluid flow using less power compared to other mechanisms, such as piezoelectric micropumps. In Section 3.2, the use of SAW devices for micro actuation is presented and discussed. Section 3.3 explains the operation of the SAW device based microactuator. The underlying theoretical model is then elaborated in Section 3.4 and followed by a method to derive the electric potential wave at the output IDT in Section 3.5. Section 3.6 shows a theoretical boundary condition analysis for the proposed model. Section 3.7 presents detailed FEM of the actuator. Then simulation results are discussed in Section 3.8. Then this is followed by a conclusion in Section 3.9.

3.2 SAW Device Based Microactuator

SAW device related technology has been utilised to design and develop MEMS based microaccelerometers and gyroscopes for military and similar applications (Varadan and Varadan 2000, Subramanian *et al.* 1997). The technology used in those applications is similar to the capacitor effect generated by programmable tapped delay lines, which use the principle of air gap coupling (Milstein and Das 1979) between the SAW substrate and a silicon superstrate; a silicon layer superimposed on the SAW device. These capacitors are then used to control the amount of RF coupling from the input IDT on the SAW substrate to the output terminal on the silicon chip (Subramanian *et al.* 1997). It is a well known method to use a sandwich structure of semiconductor on piezoelectric substrate to form the so called space–charge coupled SAW devices and SAW convolvers (Milstein and Das 1979).

Such an approach can be utilised in the design of a SAW based microactuator. The proposed approach for the actuator design is converse to the method used by Subramanian *et al.* (1997) for the microaccelerometer design. Being an elastic deformation wave on a piezoelectric substrate, the SAW induces charge separation. Thus it carries an electric field with it, which exists both inside and outside the piezoelectric substrate and decays according to Laplace's equation. In this SAW device based actuator, a thin conductive plate is placed on top of the output IDT, which is separated by an air–gap. The conductive plate does not alter the mechanical boundary conditions of the SAW substrate, but causes the surface to be equipotential and the propagating electric potential to be zero at the surface of the conductive plate. As a result, an electrostatic force is generated between the conductive plate and the output IDT in the SAW device causing micro deformations in the conductive plate.

NOTE:
This figure is included on page 51
of the print copy of the thesis held in
the University of Adelaide Library.

Figure 3.1. Rayleigh Wave Mode. Rayleigh Wave Mode which shows elliptical particle displacements (Gardner *et al.* 2001).

It is highly important to choose a suitable propagation mode for the SAW device especially when it is designed for microfluidic applications. Therefore, different acoustic modes need to be analysed. For example, one would expect horizontal shear SAW mode to be more useful than Rayleigh SAW mode. This is because when a SAW device is in vitro, Rayleigh SAW mode is rapidly damped out, due to the pressure generated by the surrounding fluid (Jones *et al.* 2008). In contrast to the general approach of using the SAW device surface to transfer the fluid, the proposed approach uses an actuator (conductive plate), which is on top of the SAW substrate. As a result the fluid flow is isolated from the SAW substrate and hence it prohibits the interaction of the fluid with the SAW mode. Moreover, Rayleigh SAW mode is best suited for space-charge related applications as most of the energy in this mode is concentrated within one wavelength of the substrate (Milstein and Das 1979), as shown in Figure 3.1. Hence, considering the measures taken to isolate the SAW substrate from the fluid in this approach, Rayleigh SAW mode was chosen.

3.3 Proposed Microactuator Operation

Figure 3.2 depicts the wireless interrogation unit for the SAW based microactuator. The actuator is made of a conductive material or alternatively, it can be made of a material such as Silicon (Si) or Silicon Nitride (Si_3N_4) and the bottom surface of the microactuator can be coated with a thin conductive material such as Gold, Platinum or Aluminium. The SAW substrate is made out of 128-YX-Lithium Niobate ($LiNbO_3$), as it is best suited for Rayleigh wave propagation.

Effectively, the output IDT and the conductive plate are used to generate an air–gap coupled SAW based electrostatic actuator. The device operation is as follows. The input IDT generates Rayleigh waves using inverse piezoelectric effect based on the RF signal that is being fed to the SAW device through the microstrip antenna. The Output IDT regenerates the electric signal using the piezoelectric effect of the SAW device. As it was explained in Section 3.2, the generated electrostatic field between this propagating electric potential wave and the conductive plate on top of the output IDT creates a compulsive and repulsive force between the two. Since the conductive plate is a thin flexural plate, it bends as a function of the applied electrostatic field enabling its use as a microactuator.

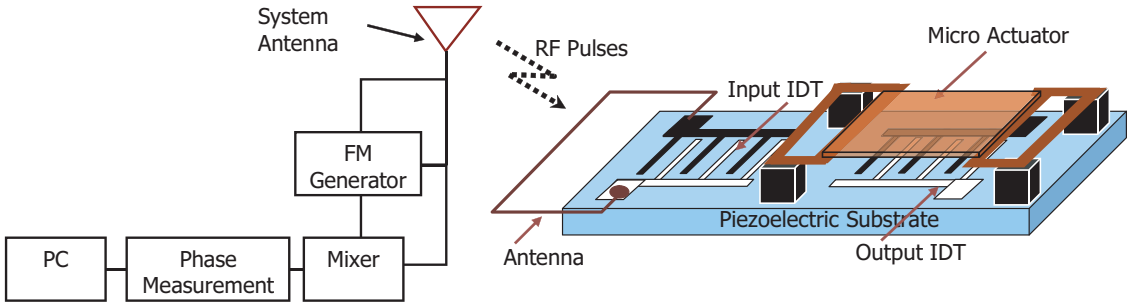

Figure 3.2. Wireless interrogation unit for SAW device based actuator. The microactuator is placed on top of the output IDT of a SAW device. SAW device consists of a piezoelectric substrate, input IDT, and output IDT. Input IDT is connected to a micro-antenna for wireless interrogation.

3.4 Theoretical Analysis of the Electrostatic Actuation

In this section, a detailed theoretical analysis is carried out to analyse the generated electrostatic force at the conductive actuator. In achieving this, first the behavior of the propagating SAW on piezoelectric media is analysed. Then the analysis is focused towards deriving a general expression for the electric potential regenerated at the output IDT of the SAW device. Additionally, a boundary condition analysis is also presented, considering a specific scenario; the placement of the conductive actuator on top of the output IDT as shown in Figure 3.3.

3.4.1 Problem Description

A variety of approaches have been followed by other researchers to investigate the SAW propagation in different piezoelectric substrates. These include, but not limited to, Potassium Niobate ($KNbO_3$), Lithium Tantalate ($LiTaO_3$), Lead Potassium Niobate ($Pb_2KNb_5O_{15}$ or PKN) (Dvoesherstov *et al.* 2000, Dvoesherstov and Chirimanov 1999), and various cuts in Lithium Niobate $LiNbO_3$ (Gardner *et al.* 2001). However, the requirement of a detailed analysis of the use of 128-XY $LiNbO_3$, specific to the novel SAW based actuator is of great importance. Therefore a descriptive theoretical analysis was carried out and presented in following sections.

In a SAW device, IDT patterns can be considered as a periodic structure. When an acoustic wave propagates on the surface through the periodic structure, it is partially reflected at each IDT finger. Depending on the operating frequency of the acoustic

wave, the reflected parts interfere constructively or destructively (Zaglmayr *et al.* 2005). Generally, these reflections are considered to be very small and therefore, in this analysis the effect of the reflections is discarded and it is assumed that a surface wave propagate through each IDT finger only once.

As can be seen from Figure 3.3, the direction of periodicity is denoted by x_1, the surface normal direction by x_3, and their perpendicular direction by x_2 following a *right-handed* coordinate system. The dimensional extension of electrodes in x_2 direction (length of the IDT fingers) is much larger in comparison to the periodicity. Additionally, a homogenous material topology is assumed in x_2 direction for this analysis.

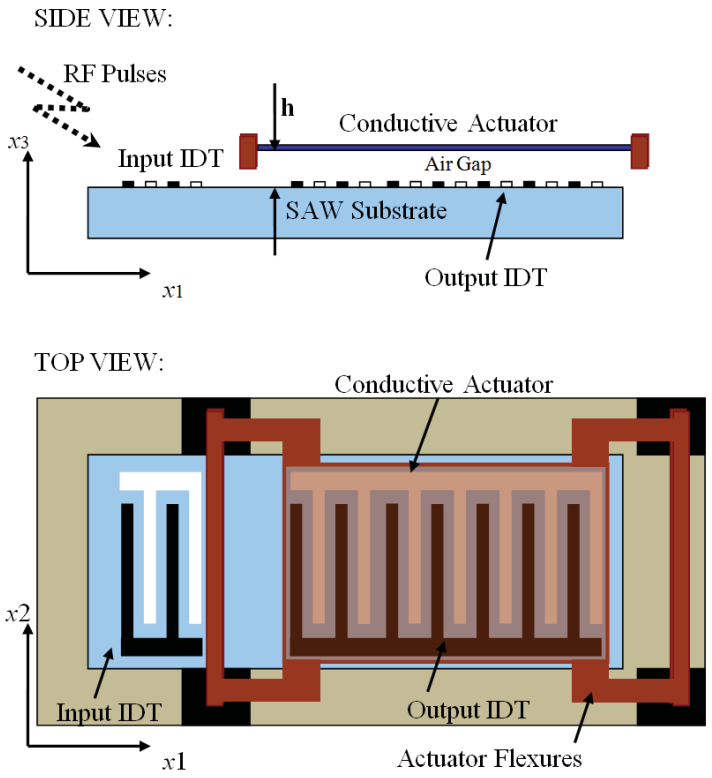

Figure 3.3. A concept drawing of the SAW actuator model. Side view: Air–gap separated conductive actuator is placed above the output IDT of the SAW device (not to scale). Top view: The actuator consists of flexures to reduce the spring constant. SAW substrate is a rotated crystal cut to make sure the wave propagation in x_1 direction and h is the height of the air gap.

3.4.2 Rayleigh Waves

In general, SAWs consist of different types of propagation modes that are considered to be 3D. However as shown in Figure 3.1, Rayleigh mode is chosen as the SAW propagation mode for this analysis, for reasons explained in Section 3.2. Rayleigh waves propagates near the surface of the piezoelectric substrate, the amplitude decreases rapidly within depth in x_3 direction, and becomes negligibly small within the depth of a few wavelengths from the surface (Zaglmayr *et al.* 2005). This behaviour is further elaborated and mathematically represented in coming sections.

The orientation of the piezoelectric material affects the SAW propagation on the substrate. Therefore, a certain crystal cut is required to direct the surface wave towards a desired direction. Here for this analysis, 128-XY $LiNbO_3$ is chosen as the substrate material due to its high electromechanical coupling coefficient (Čiplys and Rimeika 1999, Gardner *et al.* 2001). This orientation facilitate the Rayleigh mode to propagate in x_1 direction and contained in a sagittal plane define by x_1–x_3 plane. Therefore, instead of performing a full three-dimensional analysis, a model reduction is performed in the geometric domain and the analysis is carried out within the sagittal plane.

In order to derive an expression for the resultant electrostatic force, the following assumptions are made of the model and the analysis, as well as simplifications to both are mentioned. In piezoelectric materials, the frequency of the induced electric field wave is sufficiently small enough to reasonably assume the electromagnetic coupling effects to be negligible. This means that local perturbations are felt almost instantaneously through out the substrate (Gantner *et al.* 2007, Kannan 2006, Maugin 1985).

Additionally, if l is the largest characteristic dimension of the actuator structure and c is the speed of light, the generated electromagnetic coupling effects can be safely discarded, if the operating frequency of the device is much less than the ratio c/l (Zaglmayr *et al.* 2005, Horenstein *et al.* 2000). Here, for $l \sim 3$ mm, $c/l \approx 100$ GHz. Therefore, since the chosen signal frequency of SAW is in the range of 50 – 100 MHz ($\ll c/l$), electromagnetic coupling effects can be safely discarded, and hence the electric field can be treated as quasi–static.

3.4.3 Piezoelectric Equations

In piezoelectric analysis, quasi–static electric field is achieved by setting the permeability to zero, corresponding to an infinite speed of the electromagnetic wave. Using

Maxwell's equations, electromagnetic quasi–static approximation can be written as

$$E_i = -\frac{\partial \Phi}{\partial x_i}, \tag{3.1}$$

$$\nabla \cdot D = 0, \tag{3.2}$$

where E is the electric field intensity, Φ is the electric potential, D is the electric flux density (dielectric displacement) and x_i (for $i = 1, 2, 3$) shows the direction of interest as shown in Figure 3.3. Here, Equation 3.2 elaborate the fact that piezoelectric materials are insulators hence there are no free volume charges (Zaglmayr *et al.* 2005). Moreover, from the mechanical equations of motion, the relationship between the mechanical displacement u, and the mechanical stress T is given by

$$\rho \frac{\partial^2 u_i}{\partial t^2} = \sum_j \frac{\partial T_{ij}}{\partial x_i}, \tag{3.3}$$

where ρ is the density of the piezoelectric substrate. For a piezoelectric media, the relation between the mechanical strain S and mechanical displacement u can be written as

$$S_{ij} = \frac{1}{2}\left[\frac{\partial u_i}{\partial x_j} + \frac{\partial u_j}{\partial x_i}\right]. \tag{3.4}$$

In order to investigate the behaviour of the electric potential and the mechanical displacement of SAW, the constitutive equations for piezoelectric material are also need to be considered. The constitutive equations for piezoelectric material can be obtained by extending Hook's law and the electrostatic equation for the electric flux density. Therefore, the relationship between D, E, T and S in a SAW substrate can be written as

$$T_{ij} = \sum_k \sum_l c^E_{ijkl} S_{kl} - \sum_k e_{kij} E_k, \tag{3.5}$$

$$D_i = \sum_j \sum_k e_{ijk} S_{jk} + \sum_j \varepsilon^S_{ij} E_j, \tag{3.6}$$

where c_{ijkl} is the stiffness tensor for constant electric field, e_{ijk} is the piezoelectric coupling tensor (e_{kij} is the corresponding transpose tensor of e_{ijk}), ε_{ij} is the permittivity tensor for constant strain and i, j, k, l vary from 1 to 3. It should be noted that the mechanical stiffness matrix $[c]$ and the permittivity matrix $[\varepsilon]$ are symmetric. Additionally, the direct and converse piezoelectric effects are also symmetric, hence in piezoelectric matrix $[e]$, the coupling coefficients are equal for both the effects (Zaglmayr *et al.* 2005). These symmetry considerations allow the reduction of the corresponding matrices of

the material tensors; $[c]$ to a 6×6 symmetric matrix, $[\varepsilon]$ to a 3×3 symmetric matrix, and $[e]$ to a 6×3 matrix.

Equations 3.1– 3.6 lead to a system of four coupled equations, which are represented by Equations 3.7 and 3.8.

$$\sum_j \sum_k \left[e_{kij} \frac{\partial^2 \Phi}{\partial x_j \partial x_k} + \sum_l c^E_{ijkl} \frac{\partial^2 u_k}{\partial x_j \partial x_l} \right] = \rho \frac{\partial^2 u_i}{\partial t^2}, \tag{3.7}$$

$$\sum_i \sum_j \left[\varepsilon^S_{ij} \frac{\partial^2 \Phi}{\partial x_i \partial x_j} - \sum_k e_{ijk} \frac{\partial^2 u_j}{\partial x_i \partial x_k} \right] = 0. \tag{3.8}$$

This relationship between mechanical displacement and electric potential is considered in a semi–infinite, isotropic and homogenous linear elastic space as shown in Figure 3.1. As was mentioned above, the piezoelectric crystal cut ensures the Rayleigh wave propagate in the x_1-x_3 sagittal plane as shown in Figure 3.3. An alternative definition to the sagittal plane, can be given as, the plane defined by the real wave vector (wave number) k and the unit vector normal to the surface of the SAW substrate (x_3 direction).

Various approaches have been proposed by researchers to solve wave propagation on anisotropic substrates (Zaglmayr *et al.* 2005, Gantner *et al.* 2007, Adler 2000). The method of partial waves is considered to be a commonly used technique to analyse different SAW modes on anisotropic substrates such as piezoelectrics. Therefore, in this research the method of partial waves is used to solve this wave propagation phenomena for the SAW actuator model. As a result, plane wave solutions of the form given in Equations 3.9 and 3.10 are considered for the mathematical modelling of this device,

$$u^m_j(x_1, x_3, t) = \alpha^m_j e^{\mathrm{i}kb^m x_3} e^{\mathrm{i}k(x_1 - vt)}, \tag{3.9}$$

$$\Phi^m(x_1, x_3, t) = \alpha^m_4 e^{\mathrm{i}kb^m x_3} e^{\mathrm{i}k(x_1 - vt)}, \tag{3.10}$$

where the α^m_j values are linear coefficients that depend on the decaying constant b^m, v is the phase velocity of the wave, k $(= 2\pi/\lambda)$ is the wave vector, λ is the wavelength, i is the standard imaginary unit $(=\sqrt{-1})$, m = 1, 2, 3, 4 and j = 1, 2, 3.

By substituting the plane wave solutions given in Equations 3.9 and 3.10 into the coupling wave Equations 3.7 and 3.8, a linear system for the coefficients α^m_j can be obtained and solved. In solving these equations, it is necessary to transform the material

parameters of the SAW substrate to match the coordinate system of the problem. This is discussed in Section 3.4.4.

3.4.4 Transformation of Coordinates

As it was mentioned above, different crystal cuts consist of different material properties. Therefore it is significant to consider the specific orientation of the selected crystal for a specific analysis, to obtained the desired SAW mode. In the equations of motion the material parameters are expressed in terms of structural coordinate axes that are selected for convenient boundary condition and excitation requirements. However, the material parameters are presented in the form of $[c]$, $[\varepsilon]$, and $[e]$ matrices as was mentioned in Section 3.4.3, and these are expressed according to the crystalline axes. Therefore it is necessary to transform the material parameters to match the coordinate system of the problem. Generally, the parameters are transformed using a transformation matrix $[r]$ given by

$$[r] = \begin{bmatrix} \cos\psi\cos\phi & \cos\psi\sin\phi & \sin\psi\sin\theta \\ -\cos\theta\sin\phi\sin\psi & +\cos\theta\cos\phi\sin\psi & \\ \sin\psi\cos\theta & -\sin\psi\sin\phi & \cos\psi\sin\theta \\ -\cos\theta\sin\phi\cos\psi & +\cos\theta\cos\phi\cos\psi & \\ \sin\theta\sin\phi & -\sin\theta\cos\phi & \cos\theta \end{bmatrix} = \begin{bmatrix} r_{11} & r_{12} & r_{13} \\ r_{21} & r_{22} & r_{23} \\ r_{31} & r_{32} & r_{33} \end{bmatrix},$$

where the elements of this matrix are the direction cosines between the crystalline axis and the problem axis (Subramanian *et al.* 1997, Kannan 2006, Wolfram MathWorld 2009).

In this research, the X–convention is followed for specifying the order of rotation of the axes. The rotations specified by the Euler angle set that are related to the X-convention and the rotation order are explained in Figure 3.4.

Once the transformation matrix is defined, the matrices that define the crystal properties ($[c]$, $[\varepsilon]$, and $[e]$) are then transformed using the Bond–Transformation procedure (Upadhyay 2004). The advantage associated with the this procedure, for stiffness and compliance, is that Bond-Transformation is directly applied on stiffness or compliance constants given in *abbreviated subscript notation*. Therefore the transformation

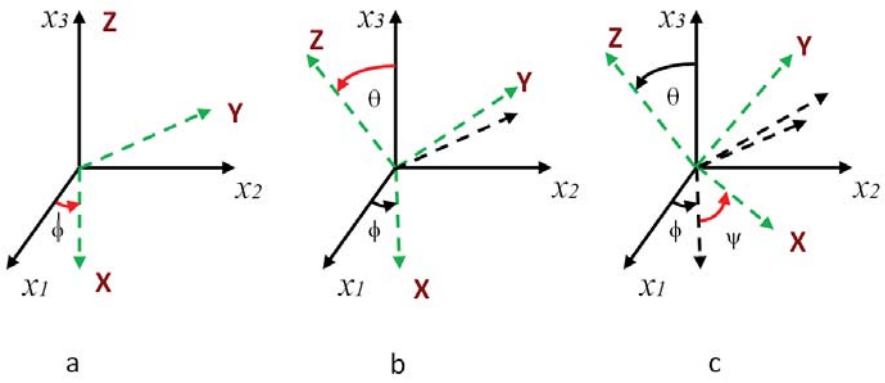

Figure 3.4. Transformation of coordinate system. Transformation of coordinate system using **X**–convention. Here $x_1x_2x_3$ is the structural coordinate system and XYZ is the crystal coordinate system. Here x_1 determines the wave propagation direction and x_3 is normal to the crystal surface. Initially both of these axes are parallel to each other. While the structural coordinate axes always remain same, the crystal axes XYZ are rotated by an angle ϕ around Z axis, then by an angle θ around X axis and finally by an angle ψ once again around Z axis. The direction cosines are then derived based on the Euler angles.

laws of this procedure can be shown as

$$[c_r] = [M_B][c][M_B{}^T], \tag{3.11}$$

$$[e_r] = [M_B][e][r^T], \tag{3.12}$$

$$[\varepsilon_r] = [r][\varepsilon][r^T], \tag{3.13}$$

where $[M_B]$ is the Bond–Transformation matrix given by

$$[M_B] = \begin{bmatrix} r_{11}^2 & r_{12}^2 & r_{13}^2 & 2r_{12}r_{13} & 2r_{11}r_{13} & 2r_{11}r_{12} \\ r_{21}^2 & r_{22}^2 & r_{23}^2 & 2r_{22}r_{23} & 2r_{21}r_{23} & 2r_{21}r_{22} \\ r_{31}^2 & r_{32}^2 & r_{33}^2 & 2r_{32}r_{33} & 2r_{31}r_{33} & 2r_{31}r_{32} \\ r_{21}r_{31} & r_{22}r_{32} & r_{23}r_{33} & r_{22}r_{33}+r_{32}r_{23} & r_{21}r_{33}+r_{31}r_{23} & r_{21}r_{32}+r_{31}r_{22} \\ r_{11}r_{31} & r_{12}r_{32} & r_{13}r_{33} & r_{12}r_{33}+r_{32}r_{13} & r_{31}r_{13}+r_{11}r_{33} & r_{11}r_{32}+r_{31}r_{12} \\ r_{11}r_{21} & r_{12}r_{22} & r_{13}r_{23} & r_{12}r_{23}+r_{22}r_{13} & r_{11}r_{23}+r_{21}r_{13} & r_{11}r_{22}+r_{21}r_{12} \end{bmatrix}.$$

$[r^T]$ denotes the transpose of the matrix $[r]$. $[c_r]$ is the transformed stiffness matrix, $[e_r]$ is the transformed piezoelectric matrix and $[\varepsilon_r]$ is the transformed permittivity matrix. These transformed matrices can be used to derive more specific partial wave equations for a certain SAW mode for a known crystal cut as shown in the following section.

3.4.5 Calculations for 128–YX–$LiNbO_3$ Substrate

It is highly important to select a piezoelectric material with high electromechanical coupling in order to maximise the signal strength of the electric potential at the output IDT of the SAW device. Therefore, 128-YX-$LiNbO_3$ is chosen for this device, as it consists of the highest electromechanical coupling efficiency for Rayleigh SAW modes, compared to other commonly used piezoelectric substrates (Čiplys and Rimeika 1999). Following the crystal transformation procedure described in Section 3.4.4, the coordinations of substrate is need to be transformed into a coordinate system defined by x_1, x_2 and x_3 as shown in Figure 3.3. This results in a new set of material parameters for the substrate, which is then used during the derivation of electric potential and mechanical displacement functions of the SAW mode.

The Euler angles associated with the crystal rotation for 128-YX-$LiNbO_3$ is $(0, 38°, 0)$, and the rotated material parameters take the general form as presented below.

$$[\boldsymbol{c_r}] = \begin{bmatrix} c_{11} & c_{12} & c_{13} & c_{14} & 0 & 0 \\ c_{12} & c_{22} & c_{23} & c_{24} & 0 & 0 \\ c_{13} & c_{23} & c_{33} & c_{34} & 0 & 0 \\ c_{14} & c_{24} & c_{34} & c_{44} & 0 & 0 \\ 0 & 0 & 0 & 0 & c_{55} & c_{56} \\ 0 & 0 & 0 & 0 & c_{56} & c_{66} \end{bmatrix}, [\boldsymbol{e_r}] = \begin{bmatrix} 0 & e_{12} & e_{13} \\ 0 & e_{22} & e_{23} \\ 0 & e_{32} & e_{33} \\ 0 & e_{42} & e_{43} \\ e_{51} & 0 & 0 \\ e_{61} & 0 & 0 \end{bmatrix}, [\boldsymbol{\varepsilon_r}] = \begin{bmatrix} \varepsilon_{11} & 0 & 0 \\ 0 & \varepsilon_{22} & \varepsilon_{23} \\ 0 & \varepsilon_{23} & \varepsilon_{33} \end{bmatrix}$$

In order to derive the specific plane wave equations for this crystal, partial wave Equations 3.9 and 3.10 are substituted into the Equations 3.7 and 3.8 with the rotated material parameters. As a result, the following Eigenvalue problem can be obtained.

$$\mathbf{M} \cdot \boldsymbol{\alpha} = 0. \tag{3.14}$$

Alternatively the above equation can be written as,

$$\begin{bmatrix} m_{11} - \rho v^2 & m_{12} & m_{13} & m_{14} \\ m_{12} & m_{22} - \rho v^2 & m_{23} & m_{24} \\ m_{13} & m_{23} & m_{33} - \rho v^2 & m_{34} \\ m_{14} & m_{24} & m_{34} & m_{44} - \rho v^2 \end{bmatrix} \begin{bmatrix} \alpha_1 \\ \alpha_2 \\ \alpha_3 \\ \alpha_4 \end{bmatrix} = 0. \tag{3.15}$$

The matrix coefficients in Equation 3.15 are shown below. It should be noted that for a 128-YX-$LiNbO_3$ crystal c_{15}, c_{16}, c_{35}, c_{36}, c_{45}, and $c_{46} = 0$. Additionally, e_{11}, e_{31}, e_{41}, e_{53},

e_{63} and $\varepsilon_{13} = 0$. Therefore as shown below, the matrix coefficients in $\mathbf{M}$ become simpler and the Eigenvalue problem expressed in Equation 3.15 becomes easier to solve.

$$\begin{aligned}
m_{11} &= c_{55}b^2 + 2c_{15}b + c_{11} &\Rightarrow\ m_{11} &= c_{55}b^2 + c_{11}\\
m_{12} &= c_{45}b^2 + (c_{14} + c_{56})b + c_{16} &\Rightarrow\ m_{12} &= (c_{14} + c_{56})b\\
m_{13} &= c_{35}b^2 + (c_{13} + c_{55})b + c_{15} &\Rightarrow\ m_{13} &= (c_{13} + c_{55})b\\
m_{14} &= e_{53}b^2 + (e_{51} + e_{13})b + e_{11} &\Rightarrow\ m_{14} &= (e_{51} + e_{13})b\\
m_{22} &= c_{44}b^2 + 2c_{46}b + c_{66} &\Rightarrow\ m_{22} &= c_{44}b^2 + c_{66}\\
m_{23} &= c_{34}b^2 + (c_{36} + c_{45})b + c_{56} &\Rightarrow\ m_{23} &= c_{34}b^2 + c_{56}\\
m_{24} &= e_{43}b^2 + (e_{41} + e_{63})b + e_{61} &\Rightarrow\ m_{24} &= e_{43}b^2 + e_{61}\\
m_{33} &= c_{33}b^2 + 2c_{35}b + c_{55} &\Rightarrow\ m_{33} &= c_{33}b^2 + c_{55}\\
m_{34} &= e_{33}b^2 + (e_{31} + e_{53})b + e_{51} &\Rightarrow\ m_{34} &= e_{33}b^2 + e_{51}\\
m_{44} &= -(\varepsilon_{33}b^2 + 2\varepsilon_{13}b + \varepsilon_{11}) &\Rightarrow\ m_{44} &= -(\varepsilon_{33}b^2 + \varepsilon_{11})
\end{aligned}$$

In order to evaluate the non–trivial solution for Equation 3.15, the Eigenvalue problem, $det\ (\mathbf{M}) = 0$, is required to be solved. This results in a system of characteristic equations for displacement amplitudes and electric potential in which the phase velocity v of the wave is used as unknown parameters. In general case, this system of characteristic equations is reduced to an eighth order polynomial in the decaying constant b for a given value of phase velocity. However, the resulting roots of b are either purely real or complex conjugate pairs. Since these roots leads to Rayleigh waves that decay with the depth along x_3, only the roots with negative imaginary parts are accepted to be consistent with the physical meaning of wave propagation in piezoelectric media (Gardner *et al.* 2001, Ippolito *et al.* 2002). There are four such roots for b (denoted as b^m for $m = 1, 2, 3, 4$) and for each such value, there exist a unique Eigenvector $\boldsymbol{\alpha}^m$. A general solutions is then obtained as a linear combination of partial waves such that each wave decays almost to zero as it shifts into the crystal depth approximately at a distance of several wavelengths from the surface ($x_3 = 0$). Furthermore, the solution consists of three displacement components u_j $(j = 1, 2, 3)$ and the electric potential Φ as described by the Equations 3.16 and 3.17.

$$u_j(x_1, x_3, t) = \left[\sum_m C_m \alpha_j^m e^{\mathrm{i}kb^m x_3}\right] e^{\mathrm{i}k(x_1 - vt)}, \tag{3.16}$$

$$\Phi(x_1, x_3, t) = \left[\sum_m C_m \alpha_4^m e^{\mathrm{i}kb^m x_3}\right] e^{\mathrm{i}k(x_1 - vt)}. \tag{3.17}$$

Additionally, during the derivation of the solution in the form of a SAW, it is assumed that the wave vector k is always parallel to the free surface, while the constant–phase

surfaces are always normal to the free surface. Furthermore, it is considered that the multiplier in Equations 3.16 and 3.17, which depends on the x_3 coordinate, determines the displacement amplitude, and the wave properties of the solution are determined by the multiplier $e^{ik(x_1-vt)}$. The weighting coefficients C_m of these plane waves are chosen to satisfy the mechanical and electrical boundary conditions at the surface of the piezoelectric substrate specific to this SAW based actuator model, which is discussed in detail in Section 3.6. But first, in Section 3.5, an expression is derived for the electric potential at the output IDT, using Equation 3.17.

3.5 Electric Potential at Output IDT

In order to determine the electrostatic field generated between the output IDT and the conductive plate, the evaluation of the electric potential at the output IDT is required. Here, once the plane wave equation is evaluated for the electric potential wave in the SAW device (Equation 3.17), an analysis is carried out to evaluate an expression for the electric potential at the output IDT. In achieving this, the following assumptions and simplification are made to the design apart from previously mentioned simplifications.

(i) The crystal cut is best set so that the SAW is directly propagating in the x_1 direction to allow an orthogonal interaction between the SAW and the output IDT.

(ii) The orientation of the IDT is such that a SAW is generated in the direction of maximum SAW–propagation speed.

(iii) The acoustic wave is assumed to pass the output IDT once, and interact with no reflections caused by impedance mismatches (Gardner *et al.* 2001, Ippolito *et al.* 2002).

(iv) The acoustic wave interact with the IDT in the near field where SAW can be treated as a travelling wave as was discussed before.

Due to the periodic nature of the propagating waves and the placement of the IDTs, the analysis is initially carried out only for a single period, and then extended to the whole structure. The single period placement of the output IDT is shown in Figure 3.5.

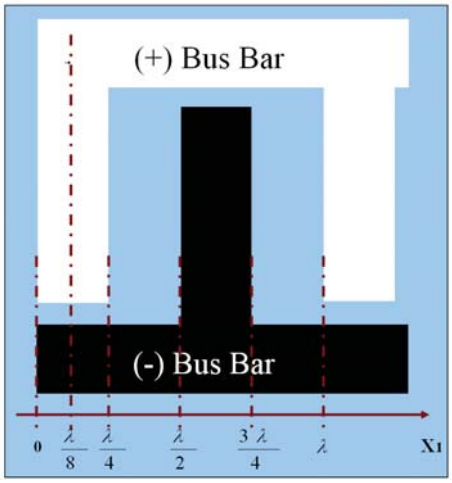

Figure 3.5. Periodic IDT finger representation. IDT finger representation for one wavelength (λ) with a metalisation ratio of $\frac{1}{2}$. Each finger is connected to one of the two bus bars, with one bus bar assigned a positive value and the other assigned a negative value.

As explained in Figure 3.5, each finger in the IDT is assigned a negative or positive value that is determined by the finger's connection to either positive or negative bus bar. Therefore, the output IDT fingers are represented as square waves with the period defining wave length of the SAW and the duty cycle defining the finger width (Skinner *et al.* 2006). This width is $\frac{\lambda}{4}$ for a metallisation ratio of 0.5. For the SAW based electrostatic actuator model, initially a basic model of the IDT configuration is used.

While the output IDT is considered as a combination of square waves, the SAW is defined as a propagating plane wave as was elaborated in Section 3.4.5. In order to obtain the time response of the SAW interaction with the output IDT, a cross–correlation is applied to the SAW and the IDT signals. Cross–correlation is a method by which two different function are compared over time with one time–fixed function and one time–shifted function. Within one wavelength of the IDT, the analysis has to be carried out in two parts, considering the space above the output IDT fingers ($0 \leq x_1 \leq \frac{\lambda}{4} \cup \frac{\lambda}{2} \leq x_1 \leq \frac{3\lambda}{4}$) and the space above the output IDT gap between fingers ($\frac{\lambda}{4} < x_1 < \frac{\lambda}{2} \cup \frac{3\lambda}{4} < x_1 < \lambda$). This is because the metal based IDT fingers consist of an equipotential distribution for a given time, and the gaps between the fingers consist of a space varying electric potential distribution in x_1 direction.

IDT Segment in Range $(0 \leq x_1 \leq \frac{\lambda}{4} \cup \frac{\lambda}{2} \leq x_1 \leq \frac{3\lambda}{4})$:

As shown in Figure 3.6, analysis of a single IDT finger will serve as the basis for the analysis for a single periodic structure and then for the entire IDT structure. Therefore, the cross-correlation between the SAW potential signal $\Phi(x_1, x_3, t)$, and the first finger connected to the positive bus bar $(0 \leq x_1 \leq \frac{\lambda}{4})$ can be expressed as

$$\begin{aligned} C_+(x_1, x_3, t) &= (\Phi * g_{(+)})(x_1, x_3, t) \\ &= \int_0^{T/4} \Phi(x_1, x_3, t+\tau) \cdot g_{(+)}(\tau) d\tau \\ &= \frac{\sqrt{2}}{kv} \Phi(x_1 - \frac{\lambda}{8}, x_3, t). \end{aligned} \tag{3.18}$$

Here, $g_{(+)}$ represents the positive square wave of the finger as can be seen from Figure 3.6.

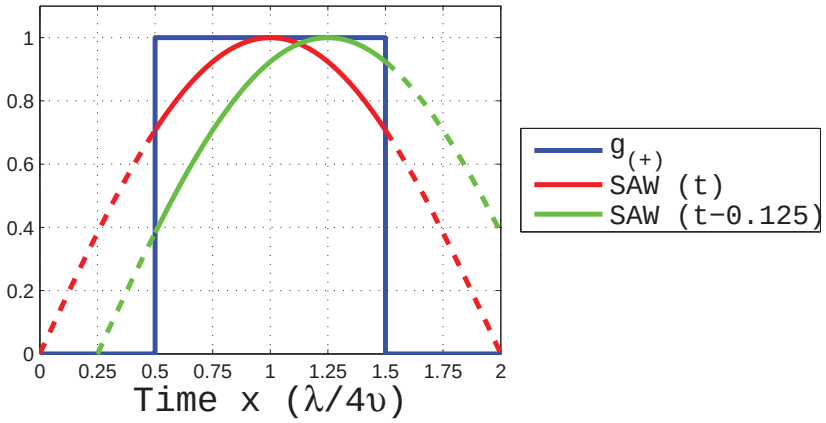

Figure 3.6. SAW and single finger correlation. Superimposition of the SAW and a single finger of the output IDT. $g_{(+)}$ represents the equipotential behaviour of the conductive finger. Two SAWs are $T/8$ apart from one another.

The electric potential at this IDT finger can be considered as the average value of the correlated signal $C_+(x_1, x_3, t)$ over the finger width f_w, due to the equipotential nature of the metal based fingers. As the metalisation ratio is 0.5 in this analysis, $f_w = \lambda/4$ and this relate to $T/4$ in time scale, where T $(= \lambda/v)$ is the time period of the SAW. Therefore, the electric potential generated at the first finger connected to the positive bus bar can be written as

$$\begin{aligned} V_+(x_1, x_3, t) &= \int_0^{\lambda/4} C_+(x_1, x_3, t) dx_1 \\ &= \frac{2T}{\pi^2} \Phi(\frac{\lambda}{8}, x_3, t). \end{aligned} \tag{3.19}$$

By following an identical approach, the electric potential at the finger connected to the negative bus bar ($\frac{\lambda}{2} \leq x_1 \leq \frac{3\lambda}{4}$) can be derived and the result can be written as

$$V_-(x_1, x_3, t) = -\frac{2T}{\pi^2}\Phi(\frac{\lambda}{8}, x_3, t). \tag{3.20}$$

IDT Segment in Range ($\frac{\lambda}{4} < x_1 < \frac{\lambda}{2} \cup \frac{3\lambda}{4} < x_1 < \lambda$):

Once the analysis is simplified by considering the aforementioned assumptions and simplifications, the electric potential at the gaps between the fingers can be considered to consist of the same electric potential of the propagating SAW as shown in Equation 3.17. Therefore

$$V_{gap}(x_1, x_3, t) = \Phi(x_1, x_3, t). \tag{3.21}$$

Based on the above analysis, the total electric potential generated by a single period of the output IDT can be expressed as

$$\Phi(x_1, x_3, t) = \begin{cases} \Psi, & for\ 0 \leq x_1 \leq \frac{\lambda}{4} \\ \Omega, & for\ \frac{\lambda}{4} < x_1 < \frac{\lambda}{2} \\ -\Psi, & for\ \frac{\lambda}{2} \leq x_1 \leq \frac{3\lambda}{4} \\ -\Omega, & for\ \frac{3\lambda}{4} < x_1 < \lambda \end{cases}, \tag{3.22}$$

where $\Psi = V_+(x_1, x_3, t) = \frac{2T}{\pi^2}\Phi(\frac{\lambda}{8}, x_3, t)$, and $\Omega = V_{gap}(x_1, x_3, t) = \Phi(x_1, x_3, t)$. This is further elaborated graphically in Figure 3.7. Consequently, due to the periodic nature of the IDT, this expression can be easily extended to derive the electric potential for the full output IDT. Therefore, for an output IDT with N_p finger pairs, the total electrostatic potential at the output IDT can be expressed as

$$\Phi(x_1, x_3, t) = \begin{cases} \Psi, & for\ n\lambda \leq x_1 \leq (\frac{1}{4}+n)\lambda \\ \Omega, & for\ (\frac{1}{4}+n)\lambda < x_1 < (\frac{1}{2}+n)\lambda \\ -\Psi, & for\ (\frac{1}{2}+n)\lambda \leq x_1 \leq (\frac{3}{4}+n)\lambda \\ -\Omega, & for\ (\frac{3}{4}+n)\lambda < x_1 < (1+n)\lambda \end{cases}. \tag{3.23}$$

Here, $n = 0, 1, 2, ..., (N_p - 1)$ and Ψ and Ω are as explained before.

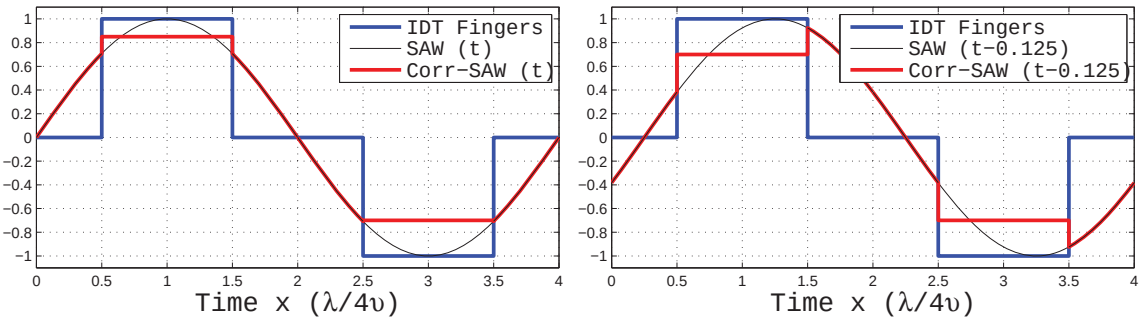

(a) time = t

(b) time = $t - T/8$

Figure 3.7. SAW correlation and the electric potential at the output IDT. Correlation between SAW electric potential and the output IDT of the SAW device is demonstrated. For a periodic IDT structure, one finger pair is represented, hence one time period ($T = \lambda/v$) is considered. Equipotential IDT fingers are represented by square waves. (a) Electric potential of the propagating SAW, $SAW(t)$ is peaked at the center of output IDT fingers (considered at time t). (b) Electric potential of the propagating SAW is $T/8$ seconds delayed compared to $SAW(t)$. In both the cases, the cross-correlated electric signal consists of equipotentials across IDT fingers.

Once the general expressions is derived, a boundary condition analysis is carried out to specify values for the weighting coefficients in Equations 3.22 and 3.23. This analysis is further unfolded in next section.

3.6 Boundary Condition Analysis

As it was highlighted above, the weighting coefficients in Equations 3.16 and 3.17 need to be determined based on the electrical and mechanical boundary conditions applicable for the SAW device based actuator model. Therefore, in this section a detailed analysis is presented to determine these weighting coefficients.

Mechanical boundary conditions:

At the output IDT area of the SAW substrate, the IDT mass is taken to be negligible for simplicity, so that the mechanical force acting on the SAW substrate can be discarded. Hence the surface is considered to be mechanically free. This can be mathematically

expressed as

$$\sum_j T_{3j} = 0, \tag{3.24}$$

where T is the mechanical stress tensor and $j = 1, 2, 3$.

Electrical boundary conditions:

In the SAW based electrostatic actuator model, the electric potential generated at the output IDT region was investigated and evaluated in Section 3.5. Based on Equation 3.23, at the surface where the output IDT is deposited ($x_3 = 0$), the electrical boundary condition constitute an electric potential at the IDT fingers, and the electric potential at the gaps between the IDT fingers. Respectively, these regions can be noted as ($0 \leq x_1 \leq \frac{\lambda}{4} \cup \frac{\lambda}{2} \leq x_1 \leq \frac{3\lambda}{4}$) and ($\frac{\lambda}{4} < x_1 < \frac{\lambda}{2} \cup \frac{3\lambda}{4} < x_1 < \lambda$) which correspond to Figure 3.5 for one period of the output IDT structure. As explained in Section 3.5, the electric potential wave at the output IDT fingers act as an equipotential time varying wave throughout the positive and negative IDT fingers (independent of x_1). Whereas the electric potential wave at the gap between the fingers, still a time varying and a moving wave (a function of x_1).

However, in the SAW device based actuator model (Figure 3.3), the conductive plate is placed at a height h above the output IDT, and connected to the common ground of the device. Therefore, the electric potential approaches zero at $x_3 = h$. It should be noted that the electric potential above the SAW substrate satisfies Laplace's equation, which results in an exponentially decaying electric signal in x_3 direction, and can be written as

$$\Phi_L(x_1, x_3, t) = \left[A_L e^{kx_3} + B_L e^{-kx_3}\right] e^{ik(x_1 - vt)}, \tag{3.25}$$

where A_L and B_L are constants. Additionally, the electric potential and the electric flux density in x_3 direction are continuous at the surface ($x_3 = 0$) (Subramanian *et al.* 1997, Maugin 1985), which can be mathematically expressed as

$$\begin{aligned} \Phi(x_3 = 0^-) &= \Phi(x_3 = 0) = \Phi(x_3 = 0^+), \\ D(x_3 = 0^-) &= D(x_3 = 0) = D(x_3 = 0^+). \end{aligned} \tag{3.26}$$

Equation 3.23 along with conditions highlighted in Equation 3.26 are considered together to eliminate both A_L and B_L in Equation 3.25. First, the electrical boundary condition at the conductive plate is considered. Since the conductive plate mounted at

a distance h above the substrate, the electric potential at $x_3 = h$ becomes zero. Therefore, from Equation 3.25,

$$\begin{aligned} \Phi_L(x_1, h, t) &= \left[A_L e^{kh} + B_L e^{-kh}\right] e^{\mathrm{i}k(x_1 - vt)} = 0, \\ B_L &= -A_L e^{2kh}. \end{aligned} \tag{3.27}$$

Once B_L is eliminated, Equation 3.25 can be rewritten as,

$$\Phi_L(x_1, x_3, t) = A_L \left[e^{kx_3} - e^{2kh - kx_3}\right] e^{\mathrm{i}k(x_1 - vt)}. \tag{3.28}$$

To evaluate the constant A_L, electrical boundary condition at the surface of the substrate ($x_3 = 0$) is need to be considered. However, as shown in Equation 3.23, the electric potential at the output IDT area is a combination of various potentials due to the output IDT and the gap between them. Therefore, two different electric potential signals have to be considered in the analysis, one considering the space above the output IDT ($0 \leq x_1 \leq \frac{\lambda}{4} \bigcup \frac{\lambda}{2} \leq x_1 \leq \frac{3\lambda}{4}$) and the other, the space above the output IDT gap ($\frac{\lambda}{4} < x_1 < \frac{\lambda}{2} \bigcup \frac{3\lambda}{4} < x_1 < \lambda$). More importantly, this distinction does not affect the final result due to the similarity in the procedure followed for the derivation of A_L. Therefore the approach is shown only for one case.

Considering the plane wave Equation 3.23 for electric potential and Equation 3.28, and the continuity Equation 3.26, A_L can be evaluated as follows,

$$\begin{aligned} \Phi_L(x_1, 0, t) &= \Phi(x_1, 0, t), \\ A_L \left[1 - e^{2kh}\right] e^{\mathrm{i}k(x_1 - vt)} &= \left[\sum_m C_m \alpha_4^m\right] e^{\mathrm{i}k(x_1 - vt)}, \text{ and} \\ A_L &= \frac{\sum_m C_m \alpha_4^m}{\left[1 - e^{2kh}\right]}. \end{aligned} \tag{3.29}$$

The relationship between the electric flux density and the electric field can be written as $D = \varepsilon_0 E$. Considering this relation along with Equation 3.1, a relationship between the electric flux density and the electric potential in the gap in x_3 direction can be written as

$$D_3(x_1, x_3, t) = -\varepsilon_0 \frac{\partial \Phi_L(x_1, x_3, t)}{\partial x_3}. \tag{3.30}$$

Hence, using the above equation, the electric flux density at $x_3 = 0$ is calculated and written as follows.

$$D_3(x_1, 0, t) = -k\varepsilon_0 \frac{\sum_m C_m \alpha_4^m \left[1 + e^{2kh}\right]}{\left[1 - e^{2kh}\right]} e^{\mathrm{i}k(x_1 - vt)}. \tag{3.31}$$

Additionally, another alternative expression for electric flux density at $x_3 = 0$ can be obtained from Equation 3.6. Therefore,

$$D_3(x_1, 0, t) = \sum_j \sum_k e_{3jk} S_{jk} + \sum_j \varepsilon^S_{3j} E_j. \tag{3.32}$$

Ultimately, by equating Equations 3.31 and 3.32, another Eigenvalue problem is formulated, where the variables consist of the weighting coefficients. The resulting boundary conditions can be written out in matrix form as follows.

$$\begin{bmatrix} \mathbb{G} & 0 & \mathbb{H} & \mathbb{I} \\ \mathbb{J} & 0 & \mathbb{L} & \mathbb{N} \\ 0 & \mathbb{P} & 0 & 0 \\ \mathbb{Q} & 0 & \mathbb{R} & \mathbb{Y} \end{bmatrix} \begin{bmatrix} C_1 \\ C_2 \\ C_3 \\ C_4 \end{bmatrix} = 0, \tag{3.33}$$

where

$$\begin{aligned}
\mathbb{G} &= (c_{13} - c_{14}b^1)\alpha_1^1 + (-c_{14} + c_{11}b^1)\alpha_3^1 + (e_{13} - e_{22}b^1)\alpha_4^1 \\
\mathbb{H} &= (c_{13} - c_{14}b^3)\alpha_1^3 + (-c_{14} + c_{11}b^3)\alpha_3^3 + (e_{13} - e_{22}b^3)\alpha_4^3 \\
\mathbb{I} &= (c_{13} - c_{14}b^4)\alpha_1^4 + (-c_{14} + c_{11}b^4)\alpha_3^4 + (e_{13} - e_{22}b^4)\alpha_4^4 \\
\mathbb{J} &= c_{44}b^1\alpha_1^1 + (c_{44} - c_{14}b^1)\alpha_3^1 + e_{51}\alpha_4^1 \\
\mathbb{L} &= c_{44}b^3\alpha_1^3 + (c_{44} - c_{14}b^3)\alpha_3^3 + e_{51}\alpha_4^3 \\
\mathbb{N} &= c_{44}b^4\alpha_1^4 + (c_{44} - c_{14}b^4)\alpha_3^4 + e_{51}\alpha_4^4 \\
\mathbb{P} &= (c_{14} + c_{66}b^2)\alpha_2^2 \\
\mathbb{Q} &= e_{51}b^1\alpha_1^1 + (e_{51} + e_{22}b^1)\alpha_3^1 - (\varepsilon_{11}b^1 + \mathrm{i}\varepsilon_0\mathbb{X})\alpha_4^1 \\
\mathbb{R} &= e_{51}b^3\alpha_1^3 + (e_{51} + e_{22}b^3)\alpha_3^3 - (\varepsilon_{11}b^3 + \mathrm{i}\varepsilon_0\mathbb{X})\alpha_4^3 \\
\mathbb{Y} &= e_{51}b^4\alpha_1^4 + (e_{51} + e_{22}b^4)\alpha_3^4 - (\varepsilon_{11}b^4 + \mathrm{i}\varepsilon_0\mathbb{X})\alpha_4^4 \\
\mathbb{X} &= \tfrac{1+e^{2hk}}{1-e^{2hk}}.
\end{aligned}$$

Here the value of $\mathbb{X}$ depends on the position of the conductive plate above the SAW device (h), and takes the value of –1 for the case where the plate is at an infinite height above the substrate ($h \longrightarrow \infty$). In this analysis, the phase velocity is explicitly present in Equations 3.16 and 3.17, and implicitly present in the roots b^m and in the linear coefficients α^m as mentioned before. Therefore a suitable value for phase velocity should be chosen for which the determinant of the coefficients in the Eigenvalue problem presented in Equation 3.33 vanishes, hence satisfy the associated boundary conditions.

It is important to realise that the above two Eigenvalue problems presented in Equations 3.15 and 3.33 are required to be solved simultaneously using iterative numerical procedures. This is due to the implicit dependency of decaying constants b^m on phase velocity v, and explicit dependency of Eigenvectors of linear coefficients α^m on v. Once

a suitable phase velocity is found, the weighting coefficients C_m can be determined. As a result, a complete solution is obtained for the electric potential at the output IDT (Equation 3.23).

3.6.1 Electrostatic Force Generation

In electrostatic actuation, the electrostatic force applied on electrostatic plates can be described using the parallel plate capacitor effect (Tsai and Sue 2007) as

$$F = \frac{1}{2}\frac{\varepsilon A \Phi^2}{(h - W_P)^2}, \tag{3.34}$$

where ε is the dielectric coefficient of the medium between the plates, A is the effective plate area, $W_P(x_1)$ is the instantaneous deflection of the actuator in x_3 direction, h is the initial plate spacing, and Φ is the applied electric potential between the plates.

In order to carry out the analysis to derive an expression for the resultant electrostatic force, the assumptions and simplifications mentioned in Section 3.4.2 are applied. Additionally, the electric field lines produced by the positive IDT fingers terminate either at the negative IDT fingers or at the conductive plate. For simplicity however, the effect of the electrostatic coupling between the IDT fingers, as well as the fringe capacitances (between the electrodes and the diaphragm), is discarded in this analysis.

Due to the periodic nature of the propagating waves and the placement of the IDTs, the electrostatic force analysis is initially carried out only for a single period, and then extended to the whole structure, similar to the electric potential calculation that is presented in Section 3.5. The single period placement of the output IDT is shown in Fig. 3.8.

Previously in Section 3.5, different segments of the output IDT were considered in analysing the electric potential at output IDT. In this section, a similar approach is followed also in analysing the electrostatic force at the output IDT. Here, within one wavelength of the IDT, the analysis is carried out in two parts; one part considering the region above the output IDT electrodes ($0 \leq x_1 \leq \frac{\lambda}{4} \cup \frac{\lambda}{2} \leq x_1 \leq \frac{3\lambda}{4}$) and other, the region above the output IDT finger gaps ($\frac{\lambda}{4} < x_1 < \frac{\lambda}{2} \cup \frac{3\lambda}{4} < x_1 < \lambda$). This is due to the fact that was proven in Section 3.5; IDT fingers consisting of an equipotential distribution for a given time instance, while the gaps between the fingers consisting of a space varying electric potential distribution in x_1 direction as shown in Equation 3.23.

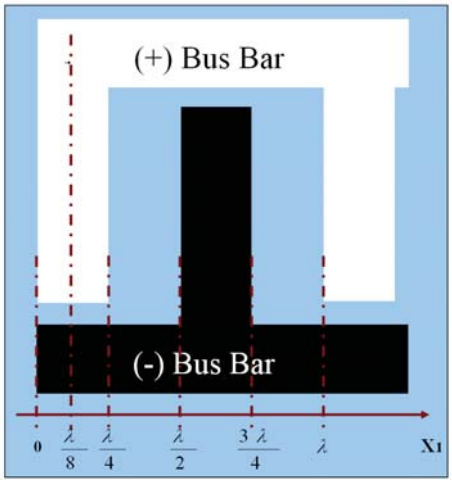

Figure 3.8. Periodic IDT finger representation. IDT finger representation for one wavelength (λ) with a metalisation ratio of $\frac{1}{2}$. Each finger is connected to one of the two bus bars, with one bus bar assigned a positive value and the other assigned a negative value.

In this analysis, an IDT with finger width of f_w and finger length of f_l is considered. For a metallisation ratio of 0.5 as in Fig. 3.8, the finger spacing is also f_w.

IDT Segment in Range $(0 \leq x_1 \leq \frac{\lambda}{4} \cup \frac{\lambda}{2} \leq x_1 \leq \frac{3\lambda}{4})$:

The electrostatic force generated by the electrode finger, which is connected to the positive bus bar $F_{(+)}$ can be evaluated considering Equations 3.23 and 3.34. As a result of the quadratic dependency of force to the applied electric potential, the force generated between the plate and the electrode finger, which is connected to the negative bus bar $F_{(-)}$ is equal to $F_{(+)}$. Therefore,

$$F_{(+)} = F_{(-)} = \frac{\varepsilon_0 f_l f_w}{2(h - W_P)^2} \left(\frac{2T}{\pi^2}\right)^2 \Phi^2(\frac{\lambda}{8}, x_3, t), \tag{3.35}$$

where ε_0 is the dielectric coefficient of air.

IDT Segment in Range $(\frac{\lambda}{4} < x_1 < \frac{\lambda}{2} \cup \frac{3\lambda}{4} < x_1 < \lambda)$:

A slightly different approach is needed to evaluate the electrostatic force generated between the conductive plate and finger gaps. This is because of the space varying electric potential distribution mentioned above. Each finger gap is divided into N_s subdivisions in x_1 direction, so that each subdivision has a width of $\frac{f_w}{N_s}$ and a length of f_l ($\approx$ aperture of the IDT). Combining the relevant range in Equations 3.23 and 3.34,

and after some algebraic simplifications, the electrostatic force generated by each gap can be evaluated as

$$F_{(gap)} = \frac{\varepsilon_0 f_l f_w}{2N_s(h - W_P)^2} \cdot \left[\sum_j \Phi^2\left(\frac{\lambda}{4} + \frac{j\lambda}{4N_s}, x_3, t\right) \right] \tag{3.36}$$

for $j = 1, 2, 3,.., N_s$. Therefore, for a distance of single wavelength (λ), the total electrostatic force generated is

$$F_{(\lambda)} = 2\left[F_{(+)} + F_{(gap)}\right]. \tag{3.37}$$

Furthermore, the above results can be used to extend the analysis to the evaluation of the resultant electrostatic force ($F_{(tot)}$) generated by an output IDT with N_p pairs of fingers. From Equations 3.35 – 3.37,

$$F_{(tot)} = \frac{C_t}{(h - W_P)^2} \sum_j \left[\left(\frac{2T}{\pi^2}\right)^2 \Phi^2\left(\frac{\lambda}{8}, x_3, t\right) + \Phi^2\left(\frac{\lambda}{4} + \frac{j\lambda}{4N_s}, x_3, t\right) \right] \tag{3.38}$$

for $j = 1, 2, 3,.., N_s$ and $C_t = \frac{\varepsilon_0 f_l f_w N_p}{N_s}$.

As the doubly–clamped actuator is deflected due to the applied electrostatic force, an elastic restoring force is developed in the actuator. At equilibrium, the kinetic energy becomes zero, and actuator's potential energy reaches to a maximum. Therefore, to determine the displacement achieved by the actuator, the calculated electrostatic force and the elastic restoring force need to be considered at their equilibrium point (Washizu 1975, Hu *et al.* 2004). However, this become a complex problem to solve since both the forces ($F_{(+)}$ and $F_{(gap)}$) depend on the actuator's instantaneous displacement $W_p(x_1)$. Therefore, to obtain an accurate solution for $W_P(x_1)$, analytical methods or numerical analysis methods such as FEA are required. Both of these methods are exploited in this research to analyse the SAW device based actuator performance.

3.6.2 The Rayleigh–Ritz Method

In order to prove the feasibility of the suggested design, and compare with the FEA results to validate the design, a reduced order model of the actuator is first built using the Rayleigh-Ritz method. Following the minimum potential energy analysis for a beam presented by Washizu (Washizu 1975), the total potential energy of the actuator, modelled in the framework of the Euler–Bernoulli theory can be deduced. For doubly–clamped actuator with a length of l, total energy E_{act} of the actuator under a pressure

P can be written as

$$E_{act} = \frac{1}{2}\int_0^l \mathbb{E}I\left(\frac{\partial^2 W_p}{\partial {x_1}^2}\right)^2 - \int_0^l PW_p dx_1, \tag{3.39}$$

where $\mathbb{E}$ is the modulus of elasticity, $W_P(x_1)$ is the lateral displacement (in x_3 direction), I is the moment of inertia of the cross section. Considering the relation, $F = P.A$, where A is the effective actuator area, the second integral component in Equation 3.39 can be rearranged using the electrostatic force, which is derived in Equation 3.38. Additionally the displacement function $W_p(x_1)$ must satisfy the essential homogeneous boundary conditions of the actuator, which is presented as follows.

$$\begin{aligned} W_p(0) &= W_p(l) = 0, \\ \frac{\partial W_p}{\partial t}\,|_{x_1=0} &= \frac{\partial W_p}{\partial t}\,|_{x_1=l} = 0. \end{aligned} \tag{3.40}$$

Even though there exist various base functions that satisfy the essential boundary conditions of the model, care was taken to select a function with a better representation of the actuator model (Bao 2000). Here, a base function for the actuator is selected as in Equation 3.41, with the only unknown being the coefficient K_P.

$$W_P(x_1) = K_P x_1^2 (l - x_1)^2. \tag{3.41}$$

As it can be seen, the function in Equation 3.41 satisfies the essential boundary conditions expressed in Equation 3.40.

In accordance with the Rayleigh–Ritz method, the equilibrium of the plate can be found by minimising the total energy E_{act} with respect to K_P. In achieving that, first total energy can be expressed in terms of K_P by substituting Equations 3.38 and 3.41 into Equation 3.39. Then the equilibrium is found from the condition

$$\frac{\partial E_{act}}{\partial K_P} = 0. \tag{3.42}$$

An iterative approach is needed until the convergence is achieved due to the complicated nonlinear coupling between Equations 3.38, 3.39 and 3.41. Actuator deformations for various operating voltages are achieved and presented in Figure 3.9. Here, it is evident that as the control signal amplitude increases the static mid–beam displacement of the actuator increases. The results based on this analytical modelling, especially the relationship between the beam deflection and the input voltage is further considered in Section 3.8.1, in validating FEM of the proposed SAW based actuator model.

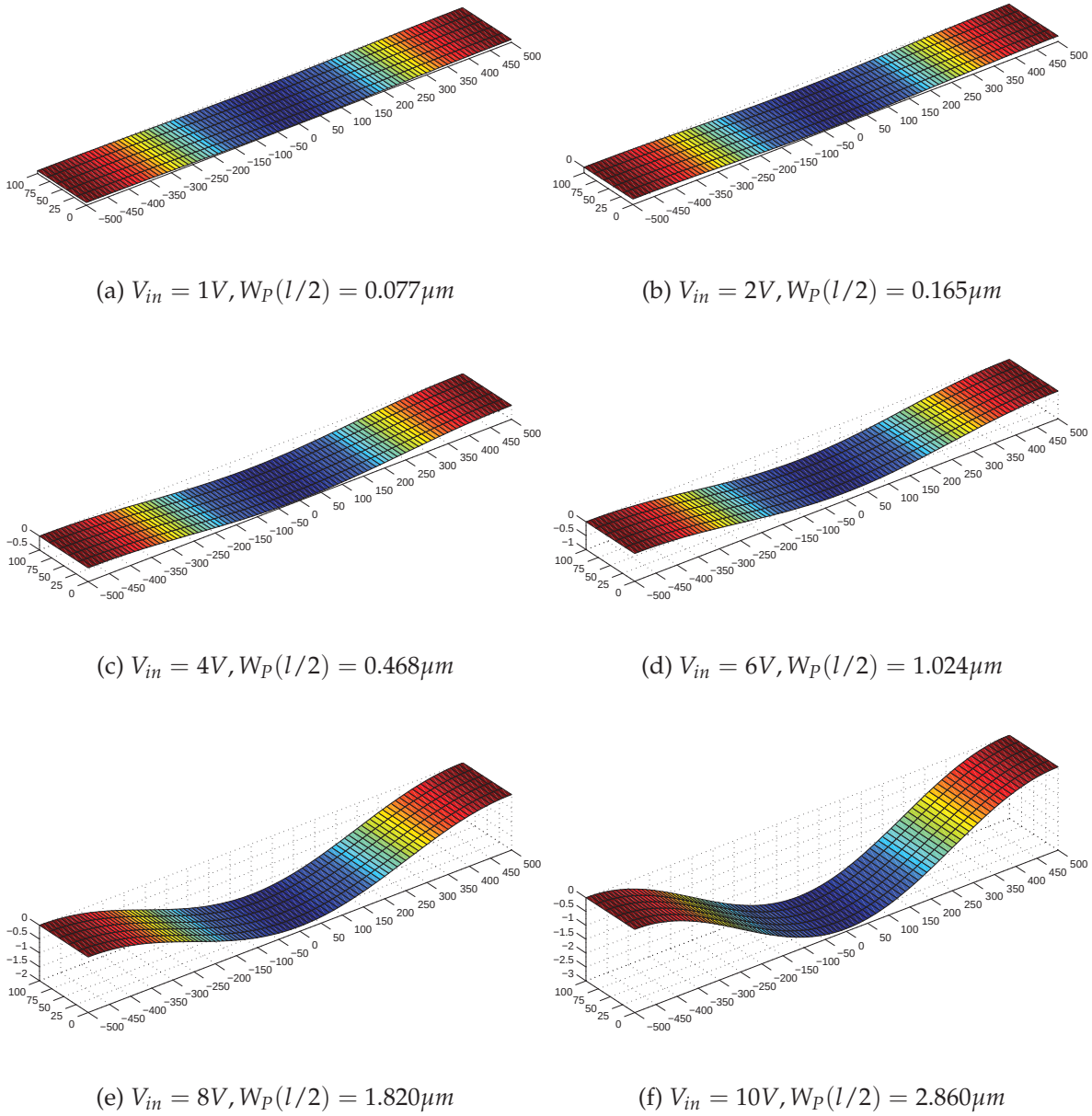

(a) $V_{in} = 1V, W_P(l/2) = 0.077\mu m$

(b) $V_{in} = 2V, W_P(l/2) = 0.165\mu m$

(c) $V_{in} = 4V, W_P(l/2) = 0.468\mu m$

(d) $V_{in} = 6V, W_P(l/2) = 1.024\mu m$

(e) $V_{in} = 8V, W_P(l/2) = 1.820\mu m$

(f) $V_{in} = 10V, W_P(l/2) = 2.860\mu m$

Figure 3.9. Actuator deflection performance. Mid–beam deflection ($W_P(l/2)$) of the actuator for different input voltages (V_{in}). As the control voltage increases, $W_P(l/2)$ increases at an increasing rate. The dimensions of the analysed actuator are 1000 μm $\times$ 100 μm (Lenght $\times$ Width).

In general, analytical approaches with lesser simplifications are quite complicated and requires extensive computational effort. It is known that more accurate results for such problems can be achieved through numerical analysis using mathematical methods such as Finite Element Analysis (FEA) (Bao 2000, Nisar *et al.* 2008b). Because of

the complexity in analysis, which involves electrostatic and structural field coupling, FEA of the microactuator is developed using ANSYS simulation tools and presented in Section 3.7.

3.7 Finite Element Modelling of the Actuator

For the Finite Element Analysis (FEA) of the actuator, a coupled–filed analysis is required since electrostatic and solid interactions are involved. Two distinct coupled–field methods can be identified in ANSYS; (i) Direct-coupling method, and (ii) Load transfer method (ANSYS Incorporation 2009a).

The direct–coupling method involves just one analysis that uses a coupled–field element type containing all necessary degrees of freedom. The coupling is handled by calculating element matrices or element load vectors that contain all necessary terms. Whereas the load transfer methods involve two or more analysis with each belonging to a different field, and two fields are coupled by applying results from one analysis as loads in another analysis.

There are different types of load transfer analysis in ANSYS; (i) ANSYS Multi–field Solver (MFS and MFX), (ii) Physics file based load transfer, and (iii) Unidirectional load transfer (ANSYS Incorporation 2009a). Suitability of these methods for a certain analysis depends on the physics fields involved, and whether the load transfer is unidirectional or not. Therefore, it is crucial to chose the most appropriate method to analyse a given scenario in order to achieve more accurate results in a reasonable simulating time. However, for MEMS applications ANSYS Multi–field solver is highly appropriate as it is a solver for sequentially coupled field analysis. Therefore in this research, ANSYS MFS is used for FEA of the SAW device based actuator.

3.7.1 Preparation of the Model for Analysis

Figure 3.10 depicts the steps that were followed in the design and modelling of this device. As it can be seen, once the geometry is created, element and material properties are defined for the actuator and the air–gap. As depicted in Figure 3.11, SOLID95 and SOLID122 element types are used for the structural and electrostatic models respectively. SOLID95 element has capabilities such as plasticity, creep, stress stiffening, large deflection, and large strain capability hence highly suitable for the design of

microactuators. Whereas, SOLID122 is a 3D, 20–node, charge based electric element, which has one degree of freedom (Voltage) at each node. It is designed to tolerate irregular shapes without much loss of accuracy. Moreover, SOLID122 elements have compatible voltage shapes and are well suited to model curved boundaries and applicable to 3D electrostatic and time–harmonic, quasi–static electric field analysis (ANSYS Incorporation 2009a). In this modelling, the effect of the output IDT is designed by coupling a set of nodes at the bottom of the air–gap to match the desired IDT pattern and assigning a Volt Degree–of–Freedom (DoF) to those nodes.

Next, the geometry is meshed to a fine level to accommodate for accurate micro level changes in the structure. Once the geometry is meshed, relevant electric and mechanical boundary conditions are applied. After setting the boundary conditions and constrains, a static analysis is carried out mainly to check for the convergence criteria. Once the results are converged in static analysis, then a model analysis is carried out to extract the natural frequencies of the conductive actuator. As a result, the operating mode for the actuator can be realised, and then a transient analysis is performed for a long enough time period that is dictated by the natural frequency mode of the actuator and the frequency of operation of the SAW device. This is an important step in the modelling process as it helps to decide on an optimal completion time for the transient analysis, since the transient simulations generally take a longer time to complete.

To simplify the analysis, the performance of the thin conductive plate with a smaller width was initially considered. Additionally, half–symmetry is exploited due to the symmetrical nature of the model. As a result, a reduced number of nodes and elements were generated for the model, and hence reduced simulation times and improved CPU usage were achieved.

3.8 Simulations and Results

3.8.1 Static Analysis

Initially, the static analysis was carried out to determine the static displacement of the actuator. In order to mimic the effect of the electric potential wave generated at the output IDT of the SAW device, a set of interleaved electrodes were used and every alternative electrode was coupled, so that one set of electrodes act as the positive bus bar and the other as the negative bus bar. Hence, in the microactuator modelling, the whole

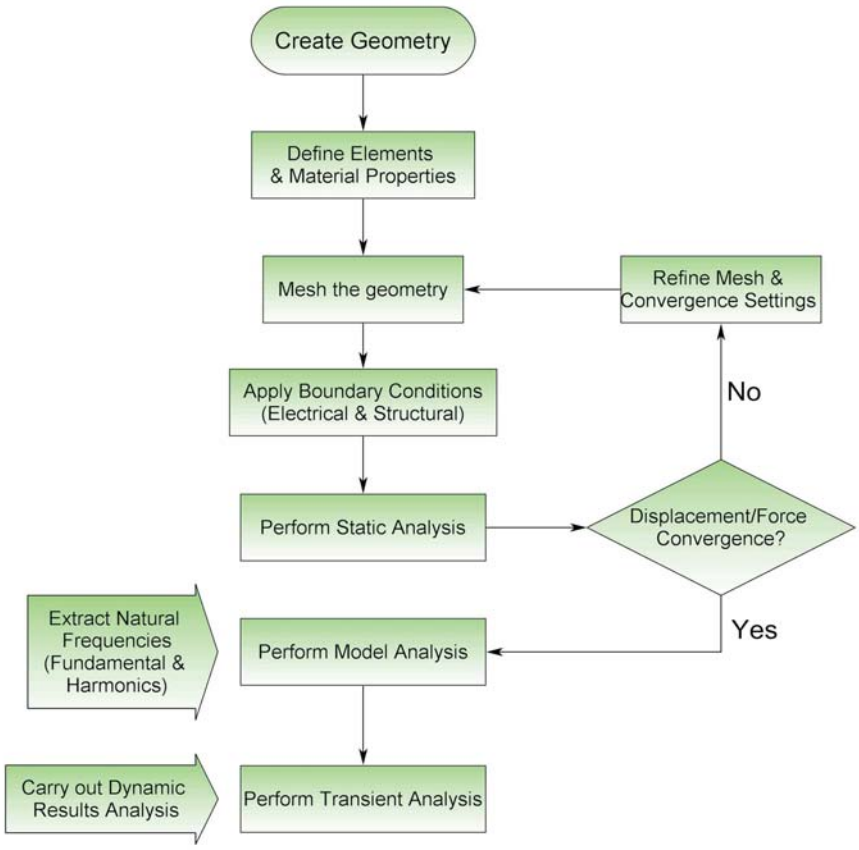

Figure 3.10. Sequential FEA flow followed in ANSYS.. The detailed steps followed in modelling of the SAW device based microactuator using ANSYS–MFS tools.

SAW device was replaced at simulation level. Material properties of silicon were used for the doubly–clamped conductive plate, which in turn acts as a microactuator. The conductive plate dimensions were chosen to be 1000 μm $\times$ 2 μm $\times$ 10 μm ($L \times H \times W$). The gap between the electrodes and the conductive plate h was taken to be 10 μm and was considered to be filled with air. For static analysis, a 10 Volt input voltage was applied to the positive bus bar. The negative bus bar and the conductive plate was connected to a common ground to form the electrostatic field.

Initial FEA results are verified using the Rayleigh–Ritz method based analytical model, which was presented in Section 3.6.2. For comparison purposes, displacement versus voltage results were plotted and are shown in Figure 3.12. A good correlation can be observed between the analytical and simulation results for the microactuator. However, FEA results demonstrate slightly lower displacements for a given voltage. This is mainly because the full thickness of the actuator was considered in the simulated 3D model in FEA, whereas the actuator was modeled as a thin plate in the Rayleigh–Ritz

NOTE:
This figure is included on page 78
of the print copy of the thesis held in
the University of Adelaide Library.

Figure 3.11. SOLID95 and SOLID122 element geometries. 3D, 20–node elements used in the design of actuator and the air–gap (ANSYS Incorporation 2009a). SOLID95 element has capabilities such as plasticity, creep, stress stiffening, large deflection, and large strain capability. SOLID122 is a charge based electric element with one degree of freedom (Voltage) at each node. SOLID122 elements are well suited to model curved boundaries and applicable to 3D electrostatic and time–harmonic quasi–static electric field analysis (ANSYS Incorporation 2009a).

method based analytical model. Therefore, the higher bending stiffness reduces the effective mid–beam displacement in the FEA model. It should be noted that the actuator displacement can be increased by reducing the gap between the conductive plate and the output IDT, reducing the thickness of the conductive plate, and reducing the stress level applied at the actuator by optimising the clamping mechanism.

Once the static analysis was completed more detailed transient analyses were performed in ANSYS to investigate the dynamic behavior of the actuator.

3.8.2 Transient Analysis

It should be noted that when a conductive beam is subject to a dynamically changing electrostatic field, the displacement behaviour needs to be calculated analytically or numerically; using advanced simulation tools equipped with in built algorithms, such as ANSYS. This section presents the transient simulation results carried out for the conductive plate with the same dimensions mentioned in the static analysis above. Moreover, an AC sinusoidal wave with a frequency of 50 MHz and a peak voltage of 10 volts were used to emulate the electric potential wave at the output IDT as proven in Equation 3.23. The conductive plate is connected to ground so that the plate acts as an equipotential surface. However, the node density of the model, and the CPU

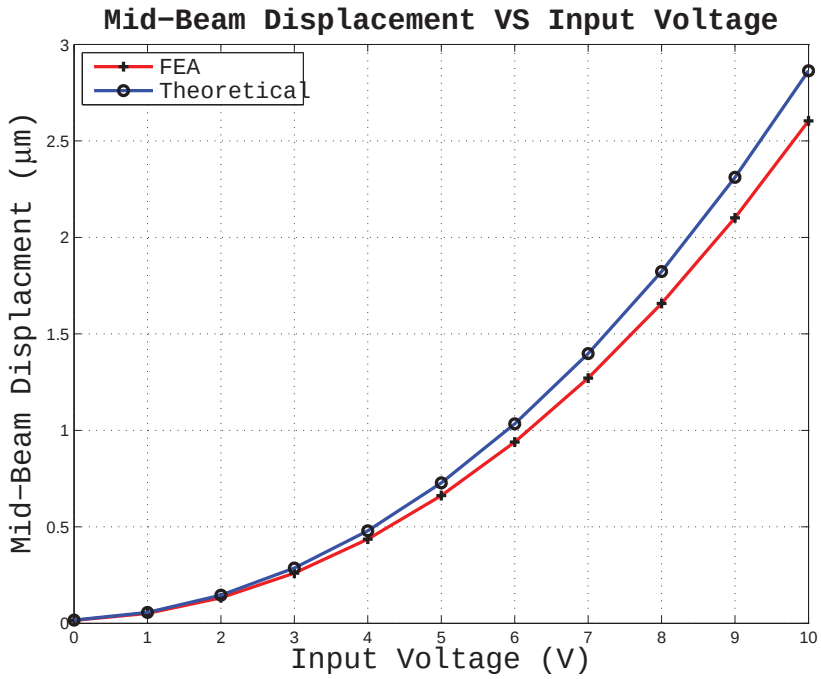

Figure 3.12. Simulation and theoretical results. Comparison of simulated and theoretical results for the SAW actuator. Displacement VS Voltage plot for the mid-beam displacement in the conductive plate actuator above the SAW device.

processing power were found to be major constrains that restricted longer transient analysis (ex: $1000 \times T$, where T is the period of SAW). Moreover, a higher node density was needed to effectively represent the output IDT in FEA model. By considering these factors, transient simulations were performed for $400 \times T$ during this analysis.

Figures 3.13 – 3.14 depict the actuator displacements for different steps in transient analysis. As a thinner actuator is modelled in ANSYS, the flexural behavior of the actuator is first observed. As the time progresses, the deflection profile of the actuator is found to be similar to the profile obtained from the Rayleigh–Ritz method based analysis (Figure 3.9 and Equation 3.41).

Figures 3.14 (c) and (d) depict the contour plot of the Von Mises stress distribution of the actuator. Here, Von Mises stress can be used to predict the yielding of any of the materials used, under any loading condition. The maximum Von Mises stress in this scenario is 0.121 MPa, which is much lower than the yield strengths of the selected material. This demonstrates that the actuator's deflection is well within the elastic range of the materials used.

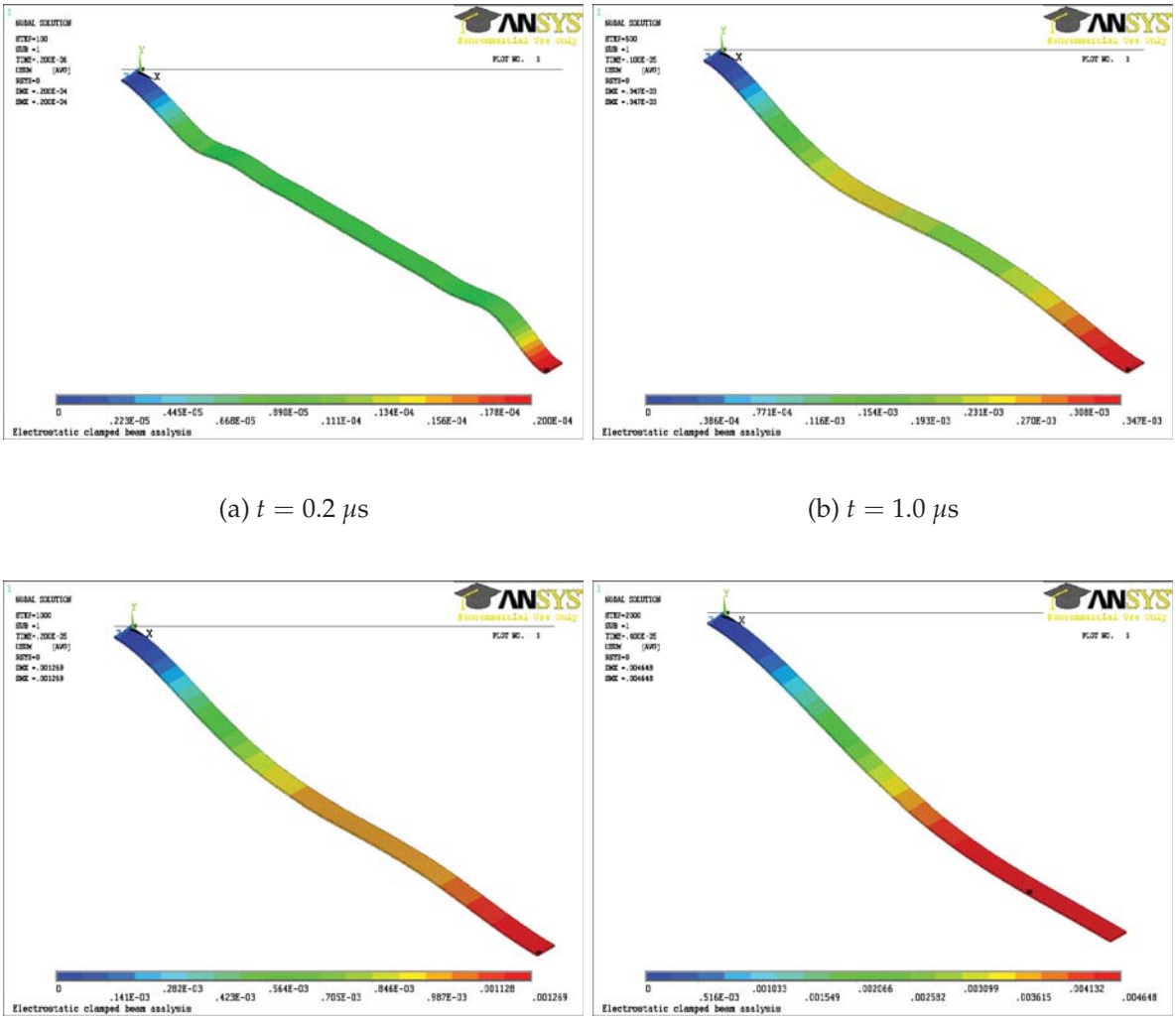

(a) $t = 0.2\ \mu$s

(b) $t = 1.0\ \mu$s

(c) $t = 2.0\ \mu$s

(d) $t = 4.0\ \mu$s

Figure 3.13. Transient analysis results for intermediate steps. Deflection results for the actuator performance at various time steps during the transient analysis. Half–symmetry is exploited due to the symmetrical nature of the model. The flexural behaviour is observed during stabilisation period.

As can be seen from these simulations, micro displacements are successfully obtained using SAW based actuation method. Figure 3.15 shows the mid–beam and the quarter–beam displacement variations over a simulation time of $400\times T$. Based on the static analysis however, it was shown that displacements up to $\sim$3 μm can be achieved using SAW device based actuation. As a result, it is proven that even after $400\times T$, still the dynamic displacement does not show any periodic nature but in the process of

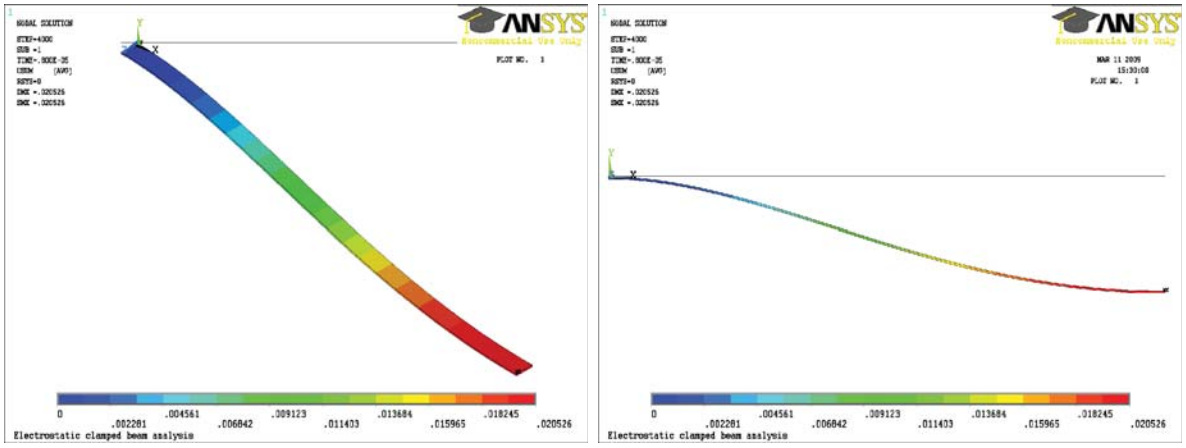

(a) Displacement, Isometric View.

(b) Displacement, Side View.

(c) Von Mises stress, Isometric View.

(d) Von Mises stress, Clamped edge.

Figure 3.14. Transient analysis results for final step. Deflection and Von Mises stress analysis results for the actuator performance at $t = 8.0$ μs. Half–symmetry is exploited due to the symmetrical nature of the model. The maximum Von Mises stress in this scenario is 0.121 MPa, which is near the clamped edge. This is much lower than the yield strengths of the selected material, hence demonstrating that the actuator's deflection is well within the elastic range.

gaining more displacement. Based on these results, it is evident that the actual operating frequency of the conductive plate during actuation is a very much a scaled down version of the SAW frequency. Furthermore, Figure 3.16 clearly depicts the existence of different deflection profiles for the SAW device based actuation. The fabricated IDT pattern dictates the actual profile characteristics of the flexural behavior.

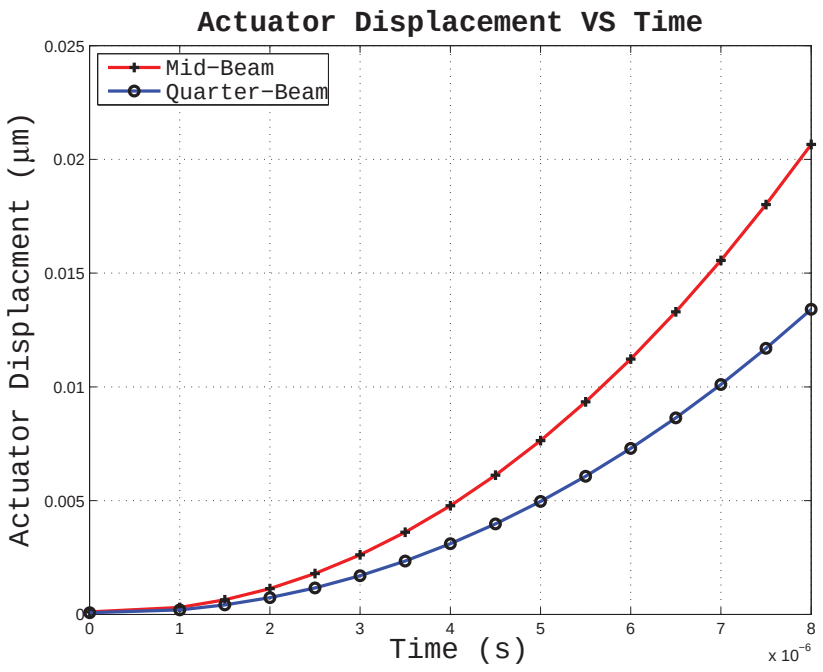

Figure 3.15. Displacement VS Time plot of the mid–beam. Analysis carried out for $400 \times T$, where T is the time period of the SAW signal. As the time increases the mid–beam displacement as well as the quarter–beam deflection increase at an increasing rate.

3.8.3 Possible Different Operating Conditions

Because of the time varying nature of the electrostatic field that is generated between the output IDT and the conductive plate, at certain operating conditions the actuator behaves as a flexural plate as it can be seen from Figure 3.17. Therefore, by increasing the frequency of the interrogating RF signal (f_{RF}) to a frequency closer to the actual SAW frequency (f_{SAW}), such that $f_{RF} \approx \frac{1}{10} \times f_{SAW}$, a flexural plate behavior can be systematically generated. Such an actuator can be used to model an ultrasonic micropump with an added advantage of better isolation between the fluidic chamber and the SAW device. Because, in previous ultrasonic micropump designs that were based on acoustic streaming principle (Miyazaki *et al.* 1991, Moroney *et al.* 1991b, Kurosawa *et al.* 1995, Nguyen *et al.* 2000b), the fluid and the SAW device is in direct contact. As a result, the SAW (mechanical travelling wave) become dampen due to the presence of fluid on the surface, and hence the magnitude of the SAW get attenuated. In contrast, by implementing the mechanism noted in this research, the damping effects on SAW mode can be negated, as the actuator isolate any fluid contact with the SAW device.

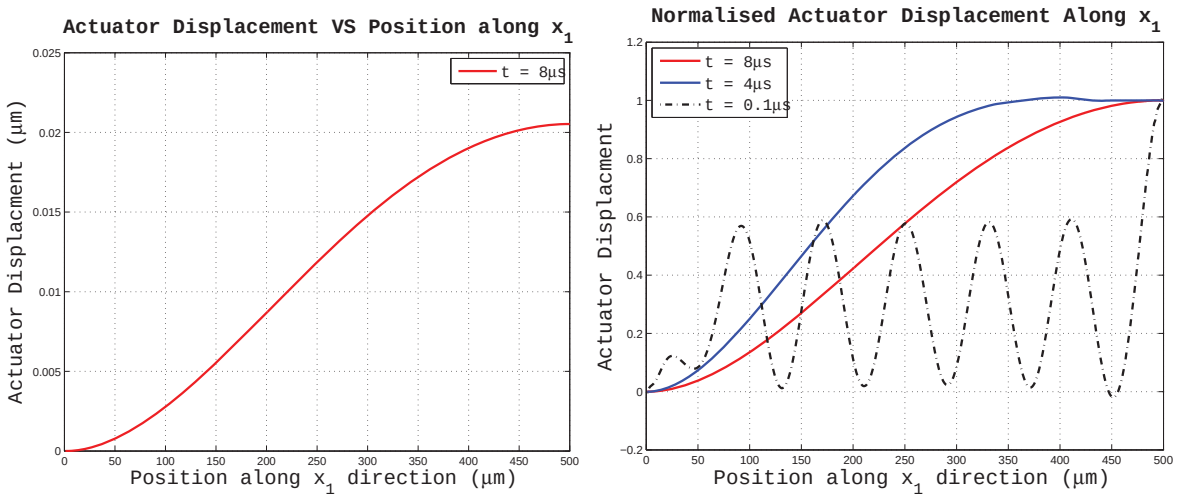

(a) (b)

Figure 3.16. Transient deflection along x_1 direction. (a) Transient analysis result demonstrating the actuator deflection along x_1 direction for final time step. (b) Normalised deflection plot is presented to show different deflection profiles at different time steps for a given operating frequency. Flexural plate behavior is clearly observed during initial steps of the simulation.

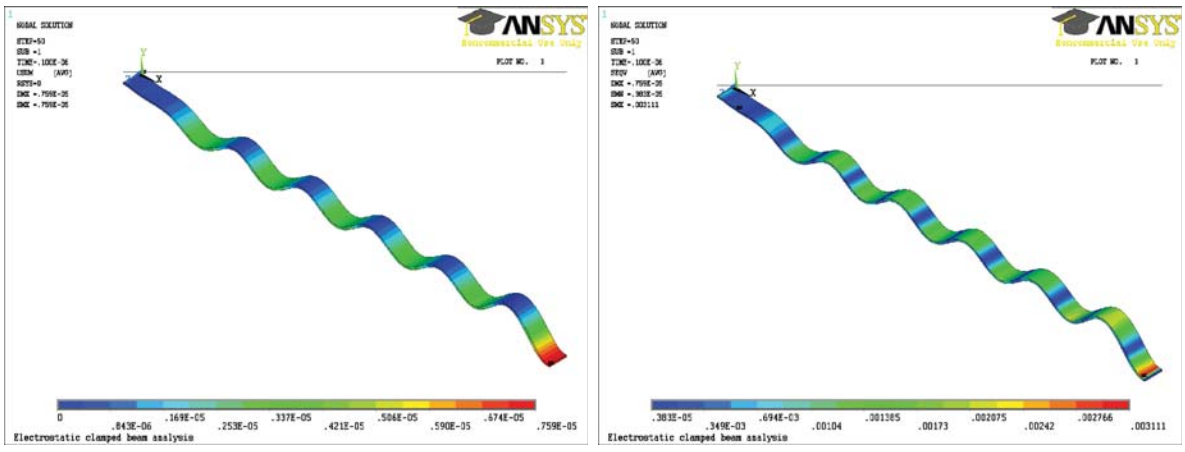

(a) Actuator deflection. (b) Von Mises stress.

Figure 3.17. Initial steps of transient analysis. Deflection and Von Mises stress analysis results for the actuator performance at $t = 0.1$ μs during the transient analysis. The flexural behaviour is clearly observed during initial stage of the simulation.

3.9 Chapter Summary

In this chapter, the use of a SAW device to generate microactuations was demonstrated. Detailed theoretical analysis explaining how the entire SAW device based actuator operation was carried out and boundary conditions applicable for presented design was used to derive the electric potential wave forms, hence the electrostatic field between the SAW device and the conductive plate. Displacement analysis of the conductive actuator was obtained. Static analysis results were generated using the ANSYS simulation tool, and compared with the theoretical results obtained by Rayleigh–Ritz method. A good correlation between the theoretical and simulated displacement curves were observed.

Once the static analysis was completed, the dynamic behaviour of the SAW device based electrostatic actuator was studied using transient analysis. This is more substantial in investigating the operating frequency of the conductive plate. Since the SAW frequency is in the range between 50 MHz–1 GHz it was crucial to verify the effective operating frequency of the conductive plate. Because of the time varying electrostatic field, it was found that the oscillating frequency of the actuator is much less than that of the SAW frequency. Furthermore, a new mechanism is presented as some potential future work, which could be used to design ultrasonic micropumps with better isolation. Based on these investigations, In Chapter 4, the SAW based actuation mechanism is further extended to model, and analyse the performance of microdiaphragms for micropumps.